An early diagenetic deglacial origin for basal Ediacaran "cap dolostones"

Anne-Sofie C. Ahm[a,*], Adam C. Maloof[a], Francis A. Macdonald[b], Paul F. Hoffman[c], Christian J. Bjerrum[d], Uyanga Bold[e], Catherine V. Rose[f], Justin V. Strauss[g], John A. Higgins[a],

[a] *Princeton University, Guyot Hall, Princeton, NJ 08540, USA*
[b] *University of California Santa Barbara, Department of Earth Sciences, Santa Barbara, CA 93106, USA*
[c] *University of Victoria, School of Earth and Ocean Sciences, BCV8W 2Y2 Canada*
[d] *University of Copenhagen, Øster Voldgade 10, 1350 Copenhagen K, Denmark*
[e] *The University of Tokyo, School of Science, Bunkyo-ku, Tokyo 113-0033 Japan*
[f] *University of St Andrews, Irvine Building, St Andrews, United Kingdom*
[g] *Dartmouth College, Fairchild Hall, Hanover, NH 03755, USA*

Abstract

The beginning of the Ediacaran Period (∼635 Ma) is marked by conspicuous dolostone units that cap Marinoan glacial deposits worldwide. The extent and sedimentary characteristics of the cap dolostones indicate that anomalous carbonate over-saturation coincided with deglacial sea-level rise and ocean warming. However, the geochemical variability within cap dolostones, both between continents, across single continental margins, and within individual stratigraphic sections has been difficult to reconcile with depositional models. Using a compilation of new calcium and magnesium isotope measurements in Marinoan cap dolostone successions worldwide, we show that the geochemical variability can be explained by early diagenetic dolomitiza-

* *Email address:* ascahm@gmail.com (Anne-Sofie C. Ahm)

tion of aragonite along a spectrum of fluid- and sediment-buffered conditions. Dolostones from the outer platform formed under fluid-buffered conditions, whereas dolostones on the inner platform and foreslope environment formed under sediment-buffered conditions. This spatial pattern of dolomitizing conditions is consistent with buoyant recirculation of glacial seawater within carbonate platforms driven by the deglacial sea-level rise and development of a meltwater surface ocean. Using a numerical diagenetic model to evaluate the geochemical differences between sediment- and fluid-buffered cap dolostone units, we constrain the chemical and isotopic composition of both the dolomitizing fluid (glacial seawater [δ^{13}C ∼0–2‰]), the meltwater lens (δ^{13}C ∼-11‰), and the primary aragonite sediment (δ^{13}C ∼-6 to -3‰). These model end-members do not imply that geochemical variability did not exist but demonstrates that it is not necessary to change the chemistry of seawater to explain the global stratigraphic variability in the geochemistry of basal Ediacaran cap dolostones. Our results provide a novel framework for understanding the geochemical variability of cap dolostone units, including large excursions in carbon isotopes, and how this variability is the product of local diagenetic processes expressed globally in continental margin environments following the last Snowball Earth.

Keywords:

Cap carbonate, Snowball Earth, Ca isotopes, Mg isotopes, Diagenesis

---

1. Introduction

In the Cryogenian Period (∼720–635 Ma), ice sheets extended to sea level in the tropics during two prolonged episodes of global glaciation (Kirschvink,

1992; Hoffman et al., 1998). The younger of these Snowball Earth events (the Marinoan) ended at ∼635 Ma and is capped by dolostone deposits that define the beginning of the Ediacaran Period (Knoll et al., 2006). These basal Ediacaran "cap dolostones" are strikingly similar across continents: they are white to buff in color with varying thickness (∼2–200 m) and contain unusual sedimentological features such as sheet-crack cements, tubestone stromatolites, and giant wave ripples (Kennedy, 1996; Hoffman and Schrag, 2002; Hoffman et al., 2007, 2011). Estimates from sedimentological studies, and some interpretations of the paleomagnetic data, suggest that the dolostones were deposited on timescales of $\sim 10^3$–10^5 yrs directly on Marinoan glaciogenic deposits during the post-glacial sea-level rise (Hoffman et al., 1998; Kennedy et al., 2001; Trindade et al., 2003; Raub, 2008). In several localities, the dolostone is conformably overlain by a limestone unit that contains the post-glacial maximum flooding surface and neomorphosed aragonite and barite fans at or above the dolostone-limestone contact (Hoffman et al., 2007, 2011). Together, the cap dolostone and overlying limestone unit constitute the Marinoan "cap-carbonate sequence" (Hoffman and Schrag, 2002; Hoffman et al., 1998).

In spite of its global extent and distinct physical appearance, the cap dolostone contains a carbon isotope excursion (CIE) that is heterogeneous both in magnitude and structure on different continents. For example, in Namibia, Death Valley, and Australia, carbon isotope values (δ^{13}C) have little stratigraphic variability within individual sections, but show a large range in δ^{13}C across each basin (∼-6 to +2‰, Hoffman, 2011; Hoffman and Macdonald, 2010; Macdonald et al., 2013b; Rose and Maloof, 2010). In contrast,

individual cap dolostone sections in Mongolia, Northwest Canada, and Arctic Alaska have large stratigraphic variation in $\delta^{13}C$ values (>3‰, Bold et al., 2016; Macdonald et al., 2009). Various hypotheses have been proposed for the origin of the cap carbonate CIE, such as turnover of a previously stratified ocean (Grotzinger and Knoll, 1995), a shutdown in biological productivity (Hoffman et al., 1998; Hoffman and Schrag, 2002), destabilization of methane hydrates following rapid warming (Kennedy et al., 2001; Jiang et al., 2003), or the combined effects of rapidly rising temperatures and CO_2-drawdown by silicate weathering (Higgins and Schrag, 2003). However, none of these hypotheses can explain the range and variability in $\delta^{13}C$ values recorded across individual continental margins and across continents.

Two models have been proposed for the origin of the Marinoan cap dolomite. Precipitation of primary dolomite is consistent with the ubiquitous dolomitic mineralogy, retention of primary fabrics (Kennedy, 1996), and the presence of coarse-grained dolomitic peloids that were reworked prior to cementation (Hoffman et al., 2011). A primary origin could imply that the cap dolostone geochemistry reflects the chemistry of the water where these sediments originally precipitated. In this model, the spatial variability in cap dolostone geochemistry would suggest either mixing of water masses across the platform (Liu et al., 2014, 2018; Yang et al., 2017) or diachronous deposition (Hoffman et al., 2007; Rose and Maloof, 2010). In the alternative model, the cap dolomite may reflect secondary dolomitization of an aragonite or calcite precursor. Due to high temperatures and pCO_2 levels, seawater chemistry in the glacial aftermath was more prone to primary precipitation of aragonite than dolomite (Fabre et al., 2013), and petrographic indicators

(growth faults, sheet veins, and multiple generations of cements) are consistent with expansive growth of cements during early diagenetic dolomitization (Gammon et al., 2012; Gammon, 2012). Early diagenetic dolomitization occurs in pore-water fluids whose chemistry reflects both the chemical composition of the original fluid (seawater, meltwater, or mixing of the two) as well as reactions that occur within the pore-fluid space (neomorphism, recrystallization, dolomitization, organic matter remineralization). According to this model, spatial and temporal variability in the geochemistry of the cap dolostone will reflect variations in the style of early diagenetic dolomitization (fluid- or sediment-buffered, Higgins et al., 2018; Ahm et al., 2018).

Calcium ($\delta^{44/40}$Ca) and magnesium (δ^{26}Mg) isotopes and major/minor element ratios (Mg/Ca and Sr/Ca) in carbonate sediments can be used to determine whether or not the Marinoan cap dolostone formed during early diagenetic alteration of aragonite or calcite. In contrast to primary dolomite precipitation, dolomites that form during early diagenesis are expected to record systematic covariation between $\delta^{44/40}$Ca values and δ^{26}Mg values that reflect formation over a range of fluid- to sediment-buffered conditions (Higgins et al., 2018; Ahm et al., 2018; Blättler et al., 2015; Fantle and Higgins, 2014). When combined with other geochemical proxies, such as δ^{13}C values, it is possible to use Ca and Mg isotopes as a geochemical fingerprint to identify fluid- and sediment-buffered dolomitization, and thereby constrain the composition of the primary sediment and the dolomitizing fluid. Here we apply this approach to the basal Ediacaran cap dolostone with new measurements of $\delta^{44/40}$Ca values, δ^{26}Mg values, and trace element ratios from 23 sections spanning four continents to determine the origin of the basal

Ediacaran cap dolostone and how its chemistry reflects conditions in the aftermath of the Marinoan glaciation.

2. Behavior of Ca and Mg isotopes during early diagenesis

Calcium in carbonate sediments and magnesium in dolomites are major components of the sedimentary mass and are inherently resistant to diagenetic alteration. However, carbonate $\delta^{44/40}$Ca and δ^{26}Mg values have been shown to be sensitive to diagenetic alteration under conditions where there is sufficient cation supply to overwhelm the calcium and magnesium in the sediment (by fluid advection or diffusion over short length-scales, Higgins et al., 2018; Fantle and Higgins, 2014; Fantle and DePaolo, 2007). For example, circulation of seawater through the Bahama Banks produces distinct covariation between $\delta^{44/40}$Ca and δ^{26}Mg values in early diagenetic dolomites (Higgins et al., 2018; Ahm et al., 2018; Fantle and Higgins, 2014). Dolomite with low $\delta^{44/40}$Ca values and high δ^{26}Mg values reflects formation under sediment-buffered conditions and retains many of the chemical signatures of the primary sediment. Dolomite with high $\delta^{44/40}$Ca values and low δ^{26}Mg values reflects formation under fluid-buffered conditions and has a chemical composition that is set by the dolomitizing fluid (seawater, Fig. 1).

Based on these observations, we interpret variability of sedimentary $\delta^{44/40}$Ca values, that are associated with covariation in δ^{26}Mg values in dolomites and Sr/Ca ratios in limestones, to be a product of change in mineralogy and early marine carbonate diagenesis (fluid- and sediment-buffered). We do not interpret these geochemical relationships in terms of changes in primary precipitation rates in the surface ocean or changes in global fluxes based on

three reasons: First, early marine diagenesis is widespread in shallow-water carbonate sediments and a plausible mechanism for the formation of large volumes of sedimentary dolomite in the geological record (e.g., Vahrenkamp and Swart, 1994). Second, although laboratory experiments have shown covariation between Sr/Ca ratios and $\delta^{44/40}$Ca values as a function of different carbonate precipitation rates (Tang et al., 2008), it is unclear if these experiments translate to natural settings. Third, given that a similar relationship between Sr/Ca ratios and $\delta^{44/40}$Ca values exists for early marine diagenesis of primary aragonite – and that this relationship has been observed and quantified during early diagenesis in modern platform settings – our model strongly suggests that covariation between the two is not a unique indicator of rate-dependence in the water column (Ahm et al., 2018). As independent geochemical and petrographic evidence exist for primary aragonite in both the cap carbonate sequence and elsewhere in the geological record (Blättler and Higgins, 2017), we regard early diagenetic alteration of aragonite as a better null hypothesis for the observed covariation between Sr/Ca ratios and $\delta^{44/40}$Ca values in ancient marine carbonate sediments.

Although we do not interpret $\delta^{44/40}$Ca values as reflecting differences in primary precipitation rates in the surface ocean, the behavior of $\delta^{44/40}$Ca values in carbonate sediments during early marine diagenesis is a consequence of the rate dependence of Ca isotope fractionation in carbonate minerals (Higgins et al., 2018; Blättler et al., 2015; Fantle and Higgins, 2014). The slow precipitation rates associated with early marine diagenesis do not appreciably fractionate Ca isotopes (Fantle and DePaolo, 2007; Jacobson and Holmden, 2008). In contrast, the precipitation rates associated with biotic and abiotic

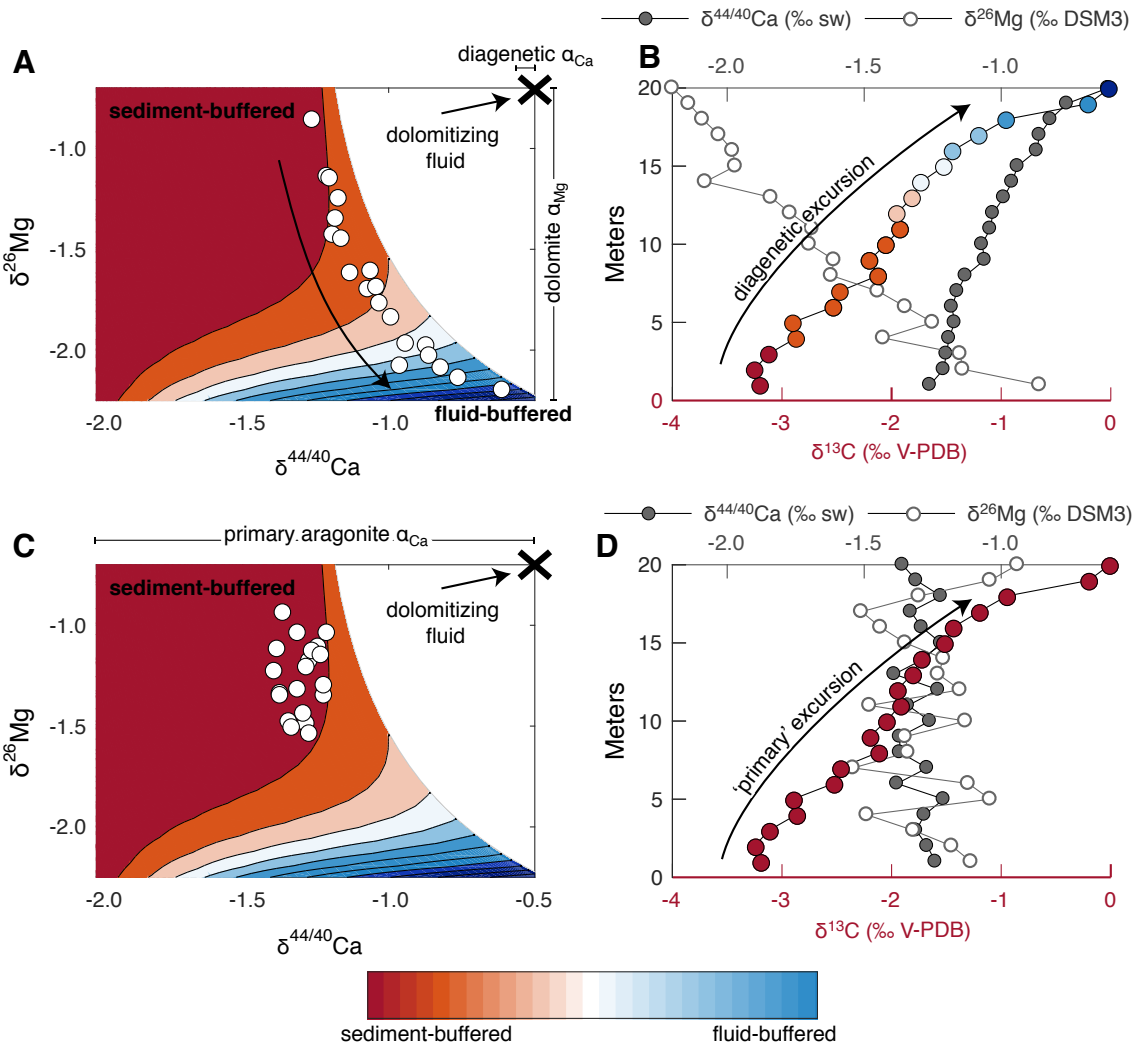
A
diagenetic α_{Ca}
sediment-buffered
dolomitizing fluid
dolomite α_{Mg}
fluid-buffered
δ^{26}Mg
$\delta^{44/40}$Ca
B
$\delta^{44/40}$Ca (‰ sw)
δ^{26}Mg (‰ DSM3)
diagenetic excursion
Meters
δ^{13}C (‰ V-PDB)
C
primary aragonite α_{Ca}
sediment-buffered
dolomitizing fluid
δ^{26}Mg
$\delta^{44/40}$Ca
D
$\delta^{44/40}$Ca (‰ sw)
δ^{26}Mg (‰ DSM3)
'primary' excursion
Meters
δ^{13}C (‰ V-PDB)
sediment-buffered
fluid-buffered

Figure 1: Schematic figure showing the combined use of $\delta^{44/40}$Ca and δ^{26}Mg values to distinguish if sedimentary δ^{13}C values have been altered or preserved during early marine dolomitization. A synthetic dataset is used to illustrate the expected $\delta^{44/40}$Ca and δ^{26}Mg isotope variability of samples that have been dolomitized during early marine fluid-buffered diagenesis (blue), and samples that have been dolomitized during sediment-buffered diagenesis (red). (A) Covariation between $\delta^{44/40}$Ca and δ^{26}Mg values, and their relationship to the δ^{13}C values, indicate that the stratigraphic trend in (B) is a product of changes in the diagenetic regime, from sediment-buffered dolomitization ($\sim$0-5 m) towards increasingly more fluid-buffered dolomitizing. (C) In contrast, low $\delta^{44/40}$Ca values and high δ^{26}Mg values indicate sediment-buffered dolomitization where the primary δ^{13}C values and stratigraphic trend (D) have been preserved. Using the modeled covariation between $\delta^{44/40}$Ca and δ^{26}Mg values, it is possible to distinguish stratigraphic trends that are primary from those that reflect changes in the diagenetic regime. Note that the specific shape of the Ca and Mg isotope phase-space is a function of the geochemistry of the primary mineral, the secondary mineral, and the diagenetic fluid (e.g., there would be a different phase-space for aragonite neomorphism or meteoric diagenesis).

precipitation of primary carbonate minerals in the surface ocean are orders of magnitude higher and can lead to significant fractionation of Ca isotope; $\sim$-1.6‰ for aragonite and $\sim$-1.1‰ for calcite (Gussone et al., 2005). Critically, the range in $\delta^{44/40}$Ca values that results from variations in carbonate mineralogy and rate-dependent Ca isotope fractionation during diagenesis are significantly larger than plausible changes in seawater $\delta^{44/40}$Ca values associated with transient perturbations to the global calcium cycle (Komar and Zeebe, 2016; Husson et al., 2015; Blättler and Higgins, 2017). Therefore, in contrast to previous studies we do not interpret Ca isotope variation in the cap carbonate sequence to reflect changes in global weathering rates (cf. Kasemann et al., 2005, 2014; Silva-Tamayo et al., 2010b,a).

The behavior of Mg isotopes during early diagenetic dolomitization is characterized by Rayleigh-type distillation of the pore-fluid due to the large fractionation factor associated with dolomite precipitation in a wide range of diagenetic environments ($\sim$-2‰, Higgins and Schrag, 2010). As magnesium is removed from the pore-fluid, the δ^{26}Mg values of the residual fluid increases, producing dolomites with yet higher δ^{26}Mg values farther along the path of fluid transport (Fig. 1). In contrast, fluid-buffered dolomites formed in pore-waters close to the origin of fluid flow will have relatively lower δ^{26}Mg values.

The systematic covariation between δ^{26}Mg and $\delta^{44/40}$Ca values in early diagenetic dolomites also provides additional insights into the origins and preservation of δ^{13}C values in carbonates rocks. As the ratio of calcium and carbon are similarly abundant in seawater and carbonates, their behavior during fluid-buffered and sediment-buffered early marine diagenesis is expected to be similar (Ahm et al., 2018). Samples where δ^{13}C values have been reset during dolomitization are expected to have high $\delta^{44/40}$Ca and low δ^{26}Mg values whereas samples where the primary δ^{13}C values of the carbonate sediment (e.g., aragonite) are preserved are expected to have low $\delta^{44/40}$Ca values and high δ^{26}Mg values (Fig. 1).

3. Background and Methods

3.1. Sample suite

Our sample suite consists of 23 stratigraphic sections from southern Africa, North America, South Australia, and Mongolia. The geological context for each section comes from previously published work that includes δ^{13}C and

δ^{18}O values (Bold et al., 2016; Hoffman et al., 2007; Hoffman and Macdonald, 2010; Hoffman, 2011; Macdonald et al., 2009, 2013b,a; Rose and Maloof, 2010) and is supplemented by new measurements from sections from northwest Canada (Strauss, unpublished). A brief summary of the settings for individual sections is outlined in Appendix A.

3.2. Methods

Ca isotope measurements from the cap carbonate sequence are reported as the relative abundance of ^{44}Ca relative to ^{40}Ca using standard delta notation, normalized to the isotopic composition of modern seawater. For Ca isotopes, the external reproducibility for SRM915b and SRM915a relative to modern seawater is -1.19 ± 0.14‰ (2σ, N=120) and -1.86 ± 0.16‰ (2σ, N=24), respectively. Similarly, Mg isotope ratios are expressed as the relative abundance of ^{26}Mg versus ^{24}Mg, normalized to DSM3 (the δ^{26}Mg value of modern seawater is -0.83‰ relative to DSM3). For Mg, the long-term external reproducibility for Cambridge-1 and seawater are -2.61 ± 0.10‰ (2σ, N=81) and -0.83 ± 0.10‰ (2σ, N=47), respectively. We refer to Appendix B and previous publications for a detailed outline of the Ca and Mg isotope analyses and major and trace element analyses performed at Princeton University (Higgins et al., 2018; Blättler et al., 2015; Husson et al., 2015).

3.3. Description of Diagenetic Model

To constrain the origin of geochemical signatures in the cap carbonates, we model carbonate diagenesis/dolomitization using a numerical model (Ahm et al., 2018). The model simulates early marine carbonate diagenesis through the dissolution of primary calcium carbonate and re-precipitation of dolomite

or low-Mg calcite along a flow path (please refer to Ahm et al. (2018) for full details on the model setup). The term neomorphism is used to describe the conversion of aragonite to low-Mg calcite, while the term dolomitization is used to describe the conversion of calcium carbonate to dolomite. Observations from modern carbonate platforms indicate that fluid flow is dominated by advection (Henderson et al., 1999; Higgins et al., 2018). We assume that the basal Ediacaran cap dolostones were dolomitized within 10^5 kyrs. This assumption implies that fluid flow and dolomitization rates were approximately an order of magnitude higher than rates estimated from modern platform environments ($\sim$0.1% kyr^{-1} and $\sim$10 cm yr^{-1}, Higgins et al., 2018; Ahm et al., 2018; Henderson et al., 1999). As a result, we set reaction rates to 1% kyr^{-1} and flow rates to 1.2 m yr^{-1}, but since we evaluate our model output in cross-plots space, our model results are not affected by changes in either reaction rates or flow rates (Ahm et al., 2018). The model output is a ternary phase-space between pairs of geochemical proxies that is defined by the geochemistry of the primary sediment, the fluid-buffered, and the sediment-buffered end-members. By identifying the fluid- and sediment-buffered end-members, we can use the model to predict the composition of the primary sediment and the diagenetic fluid.

The model is fit to the distribution of geochemical data by estimating the composition of the diagenetic fluid and primary sediment. Model results are optimized by minimizing the orthogonal difference between samples and the model phase-space (the residual). In addition, to ensure consistent predictions across different proxies, the position and shape of the model phase space is constrained by the percentage of alteration. For example, samples

that are modeled as 100% dolomitized in the phase-space of $\delta^{44/40}$Ca versus δ^{26}Mg values, should also be 100% dolomitized in the phase-space of $\delta^{44/40}$Ca versus δ^{13}C values. Samples that are less than 100% recrystallized in this model phases space are interpreted to be only partially altered during early marine diagenesis (Ahm et al., 2018). These samples are subsequently stabilized during later burial diagenesis in conditions that are sediment-buffered, thus preserving the geochemical signals associated with early marine diagenesis. In other words, our model does not assume that samples do not undergo subsequent diagenetic recrystallization (neomorphism) during burial, simply that this recrystallization must have been sediment-buffered to preserve the geochemical signature of early marine diagenesis. We refer to Appendix C for sensitivity tests and optimization of model results (Fig. C.11–C.12).

4. Results

4.1. Congo craton (Namibia)

The Keilberg cap dolostone (Hoffman et al., 2007; Hoffman, 2011) exhibits little stratigraphic variability in $\delta^{44/40}$Ca and δ^{26}Mg values within individual sections, but there are systematic trends across the Otavi platform in northern Namibia (Fig. 2). The platform interior (sections P4017 and P7500) is characterized by relatively low $\delta^{44/40}$Ca values between ∼-1 and -1.3‰ and high δ^{26}Mg values between ∼-1.5 and -1.0‰. On the outer platform (P7016), $\delta^{44/40}$Ca are consistently higher ∼-0.7‰ and δ^{26}Mg values are consistently lower ∼-1.9‰, in agreement with findings from previous studies (Kasemann et al., 2014, 2005). In contrast, a section (P7017) on the distal foreslope of the platform has $\delta^{44/40}$Ca values ∼-1‰ and δ^{26}Mg values ∼-1.7‰, a range

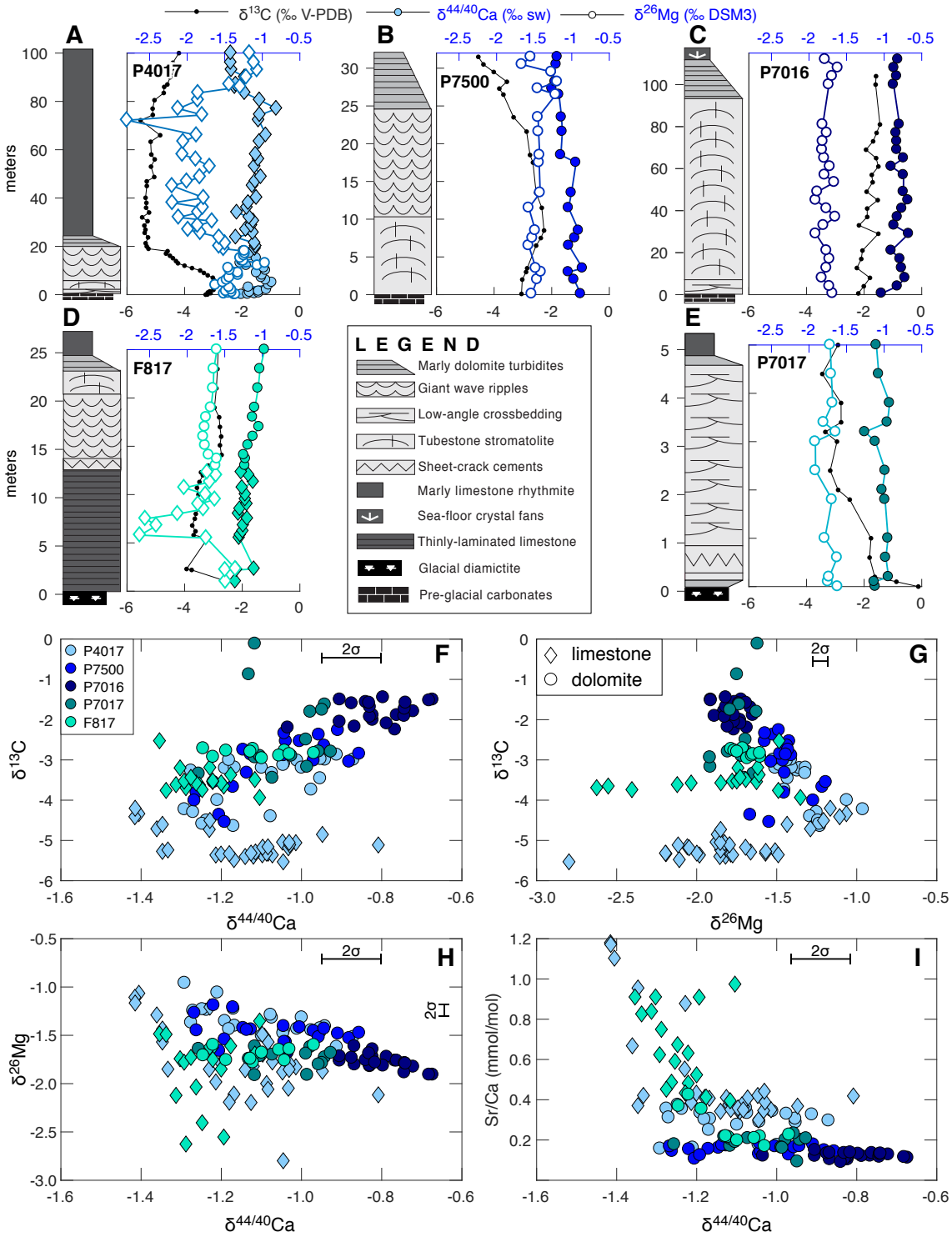
δ13C (‰ V-PDB)
δ44/40Ca (‰ sw)
δ26Mg (‰ DSM3)
A
P4017
B
P7500
C
P7016
D
F817
E
P7017
meters
LEGEND
Marly dolomite turbidites
Giant wave ripples
Low-angle crossbedding
Tubestone stromatolite
Sheet-crack cements
Marly limestone rhythmite
Sea-floor crystal fans
Thinly-laminated limestone
Glacial diamictite
Pre-glacial carbonates
F
G
H
I
2σ
limestone
dolomite
δ13C
δ44/40Ca
δ26Mg
Sr/Ca (mmol/mol)

Figure 2: (previous page) **Chemostratigraphy from the Dreigratberg and Keilberg cap carbonate, Namibia.** (A–E) Lithostratigraphy with $\delta^{44/40}$Ca, δ^{26}Mg, and δ^{13}C values from Congo craton, Namibia (P4017, P7500, P7016, P7017, Hoffman et al., 2011) and Kalahari craton, Namibia (F817, Hoffman and Macdonald, 2010). The deep water Maieberg limestones that are deposited on the Keilberg cap carbonate are included in section P4017. Sections are broadly aligned from shallow platform settings on the left towards platform margin and deeper foreslope settings on the right. (F–I) Crossplots comparing data from all five sections. Notice that circles represent dolomite and diamonds represent limestone.

similar to sections from the platform interior. Across all cap dolostone sections, there is clear positive covariation between δ^{13}C and $\delta^{44/40}$Ca values and a negative covariation between δ^{13}C and δ^{26}Mg values.

The overlying transgressive limestone unit of the Maieberg Formation (Fm.) is characterized by lower δ^{26}Mg and $\delta^{44/40}$Ca values than the dolostone (upper part of section P4017). A $\sim$1‰ decline in δ^{26}Mg values down to $\sim$-2‰ is mirrored by stratigraphic variability in $\delta^{44/40}$Ca values. $\delta^{44/40}$Ca values increase to -0.8‰ followed by a decrease down to -1.4‰. The most negative $\delta^{44/40}$Ca values in the Maieberg limestone correlate with higher Sr/Ca ratios (Fig. 2). In contrast to the underlying dolostone, in the Maieberg limestone samples with lower δ^{13}C values correlate with higher $\delta^{44/40}$Ca values and lower δ^{26}Mg values. In addition, lower $\delta^{44/40}$Ca values in the limestone covary with higher Sr/Ca ratios.

4.2. Kalahari craton (Namibia)

The Dreigratberg cap dolostone in southwest Namibia (section F817) consists of limestone overlain by dolostone (Hoffman and Macdonald, 2010). The

limestone hosts rare ice-rafted debris that marks the retreat of the ice-line and records a fall in relative sea-level prior to the surface of maximum flooding at the top of the overlying dolostone (Hoffman and Macdonald, 2010). There is no isotopic offset in $\delta^{44/40}$Ca values between the limestone and dolostone but there is a steady stratigraphic increase from -1.5 toward -1‰ towards the top of the section. In contrast, δ^{26}Mg values in the lower limestone unit record a negative excursion from -1.5 to -2.5‰. The limestone unit also has higher Sr/Ca ratios than the overlying dolostone (Fig. 2).

4.3. South Australia

The Nuccaleena cap dolostone in the Flinders Ranges, South Australia, was deposited across a large central anticline and a series of half-grabens to the north, which together span platform to basinal settings (Rose and Maloof, 2010). The Nuccaleena cap dolostone units have a large range in δ^{13}C values (between -8 and +2‰, Rose and Maloof, 2010), but a relatively small range in $\delta^{44/40}$Ca values (between ~ -1.2 and -0.7‰). Platform dolostone sections in the South and Central Flinders (N250, N255) and upper slope facies south of the Mt Fitton anticline (N288) have relatively invariant $\delta^{44/40}$Ca values (~-1‰) and δ^{26}Mg values (~-2‰) and there is broad covariation between higher Sr/Ca ratios and lower $\delta^{44/40}$Ca values (Fig. 3).

In contrast, the geochemistry of dolostone sections north of the Mt Fitton anticline are more variable with $\delta^{44/40}$Ca values between ~-1.2 and -0.7‰ and δ^{26}Mg values ~-3 and -1.6‰ (Fig. 3). Limestones deposited in upper slope facies in the shallowest part of the Mt Fitton anticline (C213) are both more enriched in ^{44}Ca (~-0.58‰) and more depleted in ^{26}Mg (~-4.4‰) relative to the basinal dolostones (C212, C215). In addition, these limestones have

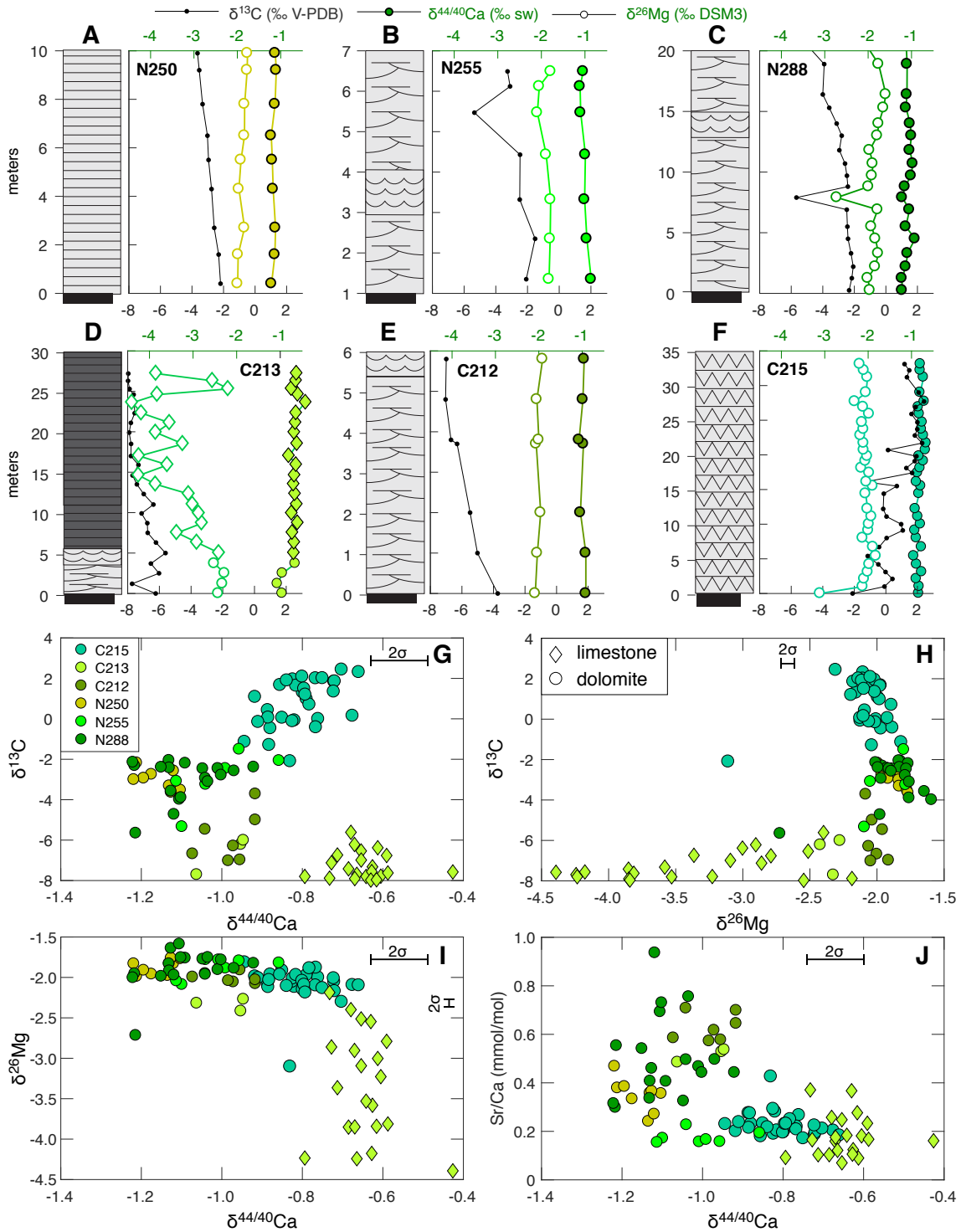
δ13C (‰ V-PDB)
δ44/40Ca (‰ sw)
δ26Mg (‰ DSM3)
A
N250
B
N255
C
N288
D
C213
E
C212
F
C215
meters
G
H
I
J
limestone
dolomite
2σ
δ13C
δ44/40Ca
δ26Mg
Sr/Ca (mmol/mol)

Figure 3: (previous page) **Chemostratigraphy from the Nuccaleena cap carbonate, South Australia.** (A–F) Lithostratigraphy with $\delta^{44/40}$Ca, δ^{26}Mg, and δ^{13}C values from south Australia (N250, N255, N288, C212, C213, C215, Rose and Maloof, 2010). For legend see figure 2. Sections are broadly aligned from shallow platform settings on the left towards platform margin and deeper foreslope settings on the right. (G–J) Crossplots comparing data from the six sections. Notice that circles represent dolomite and diamonds represent limestone.

low δ^{13}C values correlating with high $\delta^{44/40}$Ca values and low δ^{26}Mg values, whereas the dolostones have low δ^{13}C values correlating with low $\delta^{44/40}$Ca values and high δ^{26}Mg values.

4.4. Laurentia (Death Valley)

The Noonday cap carbonate (the Sentinel Peak Member) is dolomitized on the platform but is preserved as limestone in deeper foreslope settings (Silurian Hills, Macdonald et al., 2013a). In general, the platform dolostone (F1344) has higher $\delta^{44/40}$Ca values and lower δ^{26}Mg values than the deeper water limestones (F1340) and associated dolostone olistoliths (F1341). In contrast to the low δ^{26}Mg values and high $\delta^{44/40}$Ca values in the Nuccaleena limestones, the deepwater Noonday limestones have the highest δ^{26}Mg values (up to ∼-0.6‰) and the lowest $\delta^{44/40}$Ca values (down to ∼-1.9‰). In addition, the low $\delta^{44/40}$Ca values in the limestone correlate with high Sr/Ca ratios (Fig. 4).

4.5. Laurentia (Arctic Alaska)

The Nularvik cap dolostone (F601) has δ^{13}C values between 0 and -2‰ (Macdonald et al., 2009). The δ^{13}C values are inversely correlated with

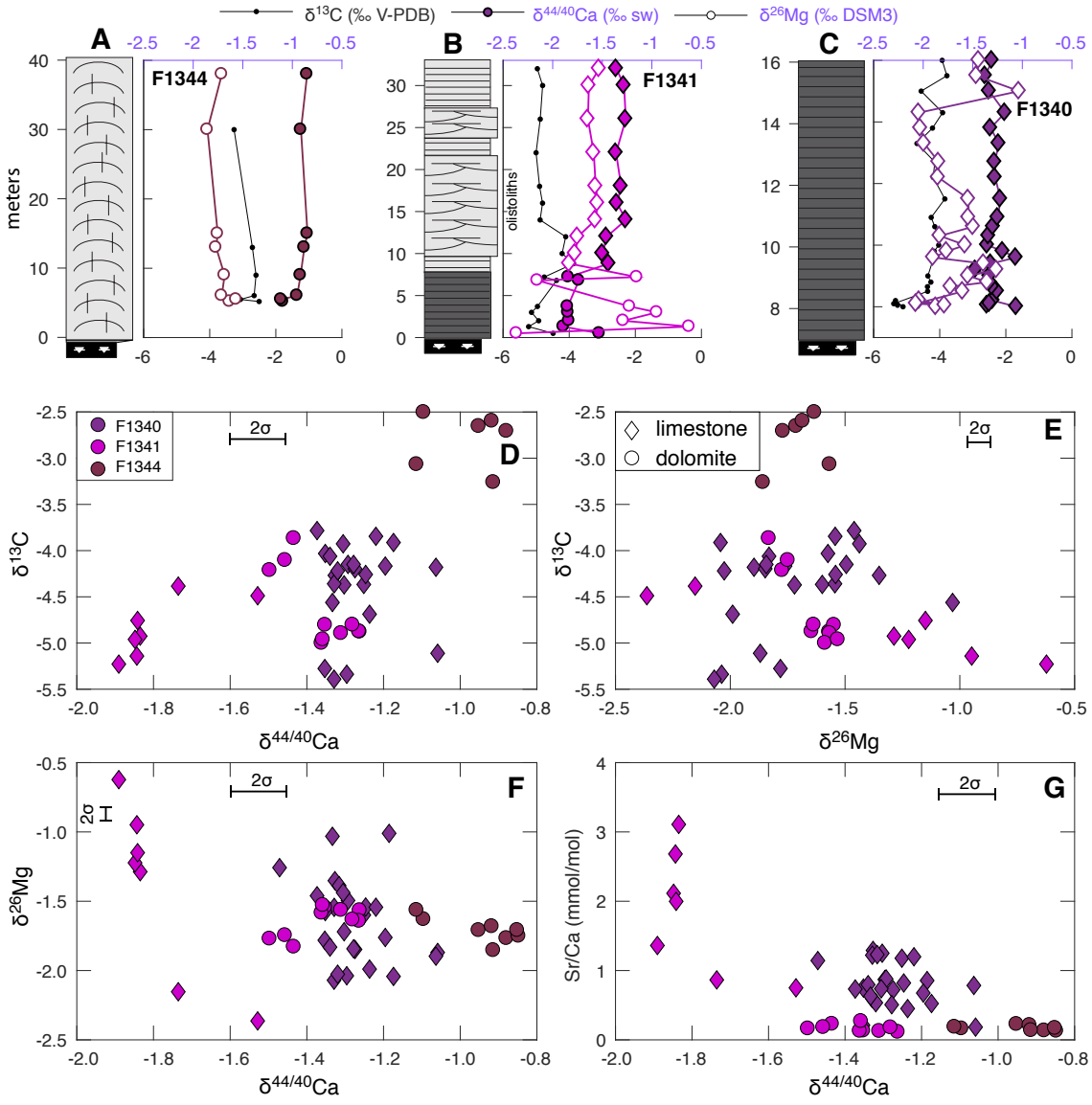

Figure 4: **Chemostratigraphy from the Noonday cap carbonate, Death Valley, California.** (A–C) Lithostratigraphy with $\delta^{44/40}$Ca, δ^{26}Mg, and δ^{13}C values from Death Valley (F1344, F1341, F1340, Macdonald et al., 2013a). For legend see figure 2. Sections are broadly aligned from shallow platform settings on the left towards platform margin and deeper foreslope settings on the right. (D–G) Crossplots comparing data from the three sections. Notice that circles represent dolomite and diamonds represent limestone.

$\delta^{44/40}$Ca values between -1.3 and -0.8‰ (Fig. 5E), while δ^{26}Mg values are relatively invariable between -2 and -1.7‰.

4.6. Laurentia (Northwest Canada)

The δ^{13}C values in the Ravensthroat cap dolostone in the Mackenzie Mountains (J1132, P7D, Macdonald et al., 2013b), Ogilvie Mountains (J1713), and Tatonduk region (J1402, Strauss, unpublished) span a range from ∼-7 to 0‰. The values in the overlying Hayhook limestone unit are less variable (∼-5‰). In contrast to the δ^{13}C values, $\delta^{44/40}$Ca values are more variable in the limestone unit (between -2 and -0.6‰) than in the underlying dolostone (between ∼-1.2 and -0.6). Similarly, the δ^{26}Mg values in the limestone span a larger range (between -3 and -1‰) than in the dolostone (between -2 and -1.3‰). As a result, there is a more pronounced covariation between δ^{13}C, δ^{26}Mg, and $\delta^{44/40}$Ca values in the dolostone compared to the limestone (Fig. 5).

Hayhook Aragonite fans. In the Mackenzie Mountains, the lowest $\delta^{44/40}$Ca values (∼-2‰) are found in calcite pseudomorphs after aragonite fans in the limestones of the Hayhook Fm. (AF; Fig. 5). $\delta^{44/40}$Ca values down to -2‰ and elevated Sr/Ca ratios rarely are found in carbonate rocks between ∼3–0.5 Ga (Blättler and Higgins, 2017), matched only during the recovery of the Ediacaran Shuram-Wonoka CIE (Husson et al., 2015). Targeted sampling of the fans and the infilling matrix reveal a consistent offset in the geochemical signature of these two texturally distinct phases. The grey fans have lower $\delta^{44/40}$Ca values, higher δ^{13}C, and lower δ^{26}Mg values than the pink mud matrix (Fig. A.10). The trace element ratios also are offset between fans

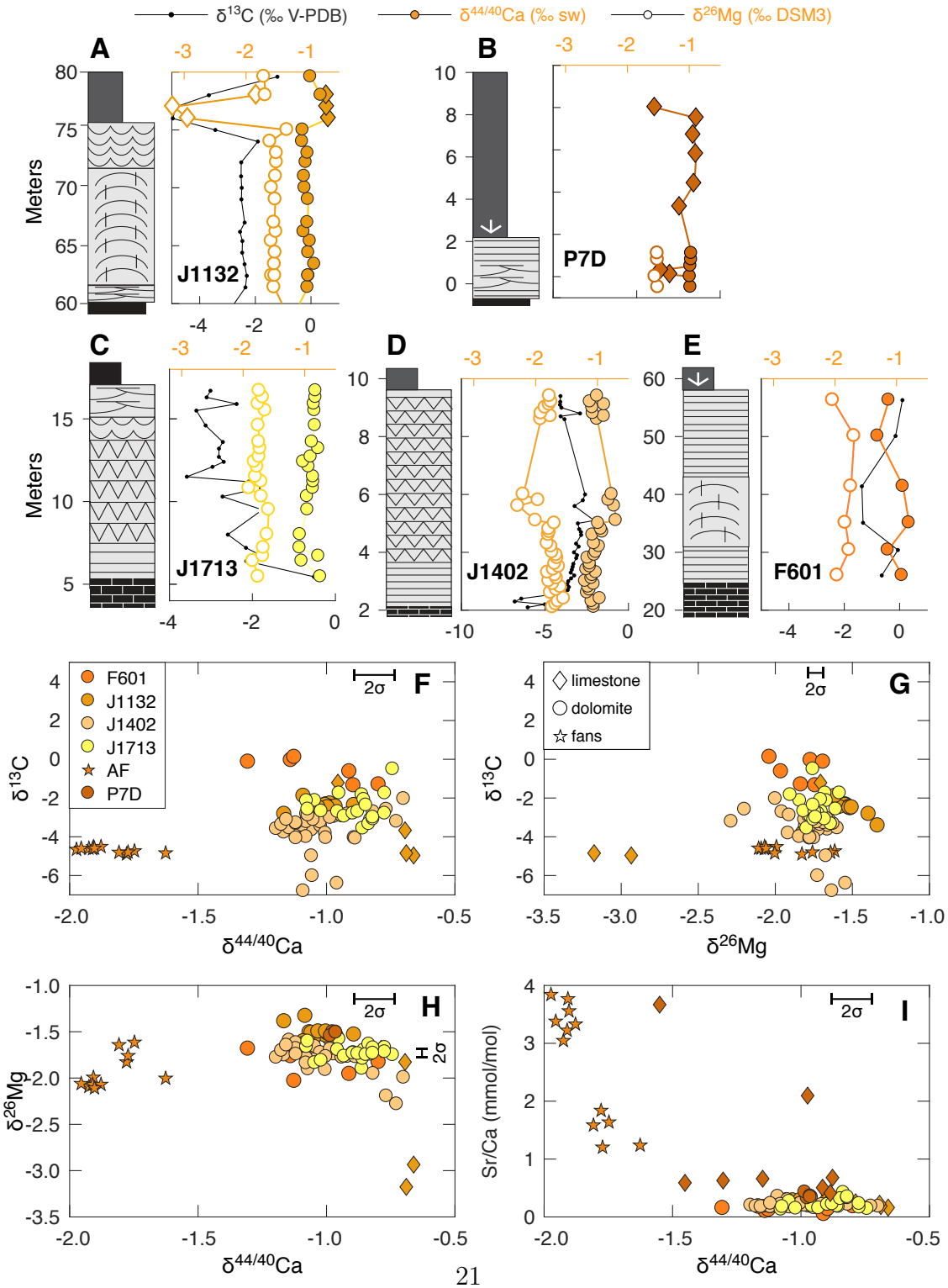
δ13C (‰ V-PDB)
δ44/40Ca (‰ sw)
δ26Mg (‰ DSM3)
A
B
C
D
E
Meters
J1132
P7D
J1713
J1402
F601
F
G
H
I
2σ
F601
J1132
J1402
J1713
AF
P7D
limestone
dolomite
fans
δ13C
δ44/40Ca
δ26Mg
Sr/Ca (mmol/mol)

Figure 5: (Previous page) **Chemostratigraphy from the Ravensthroat cap carbonate, Northwest Canada and Alaska.** (A–B) Lithostratigraphy with $\delta^{44/40}$Ca, δ^{26}Mg, and δ^{13}C values from Northwest Canada, where the Ravensthroat cap dolomites are overlain by limestones from the Hayhook Formation (J1713, J1132, P7D, J1402, Macdonald et al., 2013b), and (C–D) from Arctic Alaska (F601 Macdonald et al., 2009). For legend see figure 2. (E–H) Cross-plots comparing data from the four sections. Notice that circles represent dolomite, diamonds represent limestone, and stars represent aragonite fans.

and matrix, with higher Sr/Ca ratios and lower Mg/Ca ratios in the fans compared to the matrix.

4.7. Mongolia

In Mongolia, δ^{13}C values of the Ol cap dolostone span ∼10‰ across the Zavhkhan Terrane (Fig. 6, Bold et al., 2016). The highest values are found in sections from the inner platform (F875, U1113) that are more pervasively dolomitized than the basinal sections (Bold et al., 2016). In general, these platform sections also have higher $\delta^{44/40}$Ca values (up to -0.8‰) and lower δ^{26}Mg values (down to -2‰). In contrast, in the basinal sections (F708, F860), $\delta^{44/40}$Ca values are variable between -1 and -1.5‰, whereas δ^{26}Mg values are relatively invariant between -1.5 and -1.7‰. Combined, δ^{13}C values covary with δ^{26}Mg values across all sections with a less clear relationship between δ^{13}C and $\delta^{44/40}$Ca values. In addition, $\delta^{44/40}$Ca values do not seem to show any distinctive correlation to Sr/Ca ratio, in contrast to trends from other localities.

The geochemical signature of cap dolostone samples from Mongolia are consistently offset from sections in Australia, Namibia, and North America. Specifically, the δ^{13}C values of the Mongolian samples are higher than in other

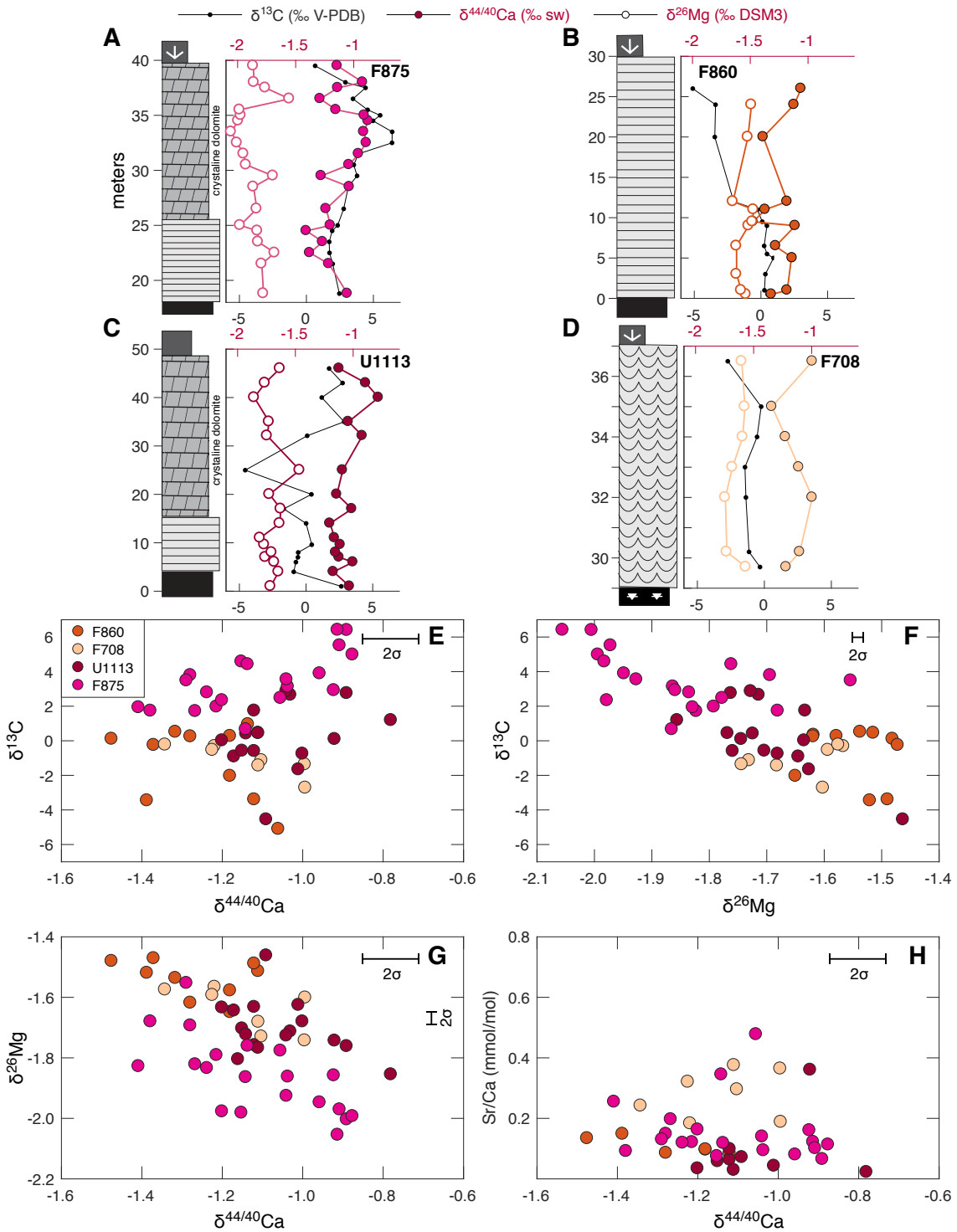
δ13C (‰ V-PDB)
δ44/40Ca (‰ sw)
δ26Mg (‰ DSM3)
A
F875
meters
crystaline dolomite
B
F860
C
U1113
crystaline dolomite
D
F708
F860
F708
U1113
F875
E
2σ
δ13C
δ44/40Ca
F
2σ
δ13C
δ26Mg
G
2σ
2σ
δ26Mg
δ44/40Ca
H
2σ
Sr/Ca (mmol/mol)
δ44/40Ca

Figure 6: (Previous page) **Chemostratigraphy from the Ol cap carbonate, Mongolia.** (A–D) Lithostratigraphy with $\delta^{44/40}$Ca, δ^{26}Mg, and δ^{13}C values from Mongolia (F875, U1113, F708, F860, Bold et al., 2016). For legend see figure 2. Sections are broadly aligned from shallow platform settings on the left towards platform margin and deeper foreslope settings on the right. (E–H) Crossplots comparing data from the four sections

sections (up to +8‰, Fig. 6). The range in values observed in Mongolia has been linked to a regionally expansive dolomitization front that penetrates the basal Ediacaran dolostone and underlying glacial and pre-glacial sediments (Bold et al., 2016). We therefore attribute the enriched δ^{13}C values in the Mongolia cap dolostone to the local history of dolomitization and fluid flow (Bold et al., 2016). Discussion of the origin of the Ol cap carbonate is limited to the supplementary material and is not discussed further below.

5. Discussion

Despite the geochemical heterogeneity between and within individual margins, $\delta^{44/40}$Ca and δ^{26}Mg values in the cap dolostone covary across all localities – dolostones with low $\delta^{44/40}$Ca values have high δ^{26}Mg values and dolostones with high $\delta^{44/40}$Ca values have low δ^{26}Mg values (Figs. 8–9). This covariation is similar to observations from Neogene dolomites (Higgins et al., 2018; Blättler et al., 2015) and is consistent with formation of early diagenetic dolomite formed under a range of diagenetic conditions (fluid- to sediment-buffered, see section 2). The appearance of similar covariation in cap dolostone units from across the globe provides evidence that cap dolostones formed by the early diagenetic conversion of a precursor carbonate

mineral and not by primary precipitation from the surface ocean (Fig. 1). In subsequent sections, we explore the implications of this result using the bulk geochemistry of carbonate sediments ($\delta^{44/40}$Ca, δ^{26}Mg, δ^{13}C values, and Sr/Ca ratios) together with a numerical model of early marine diagenesis to characterize the chemistry and isotopic composition of the primary carbonate minerals and the diagenetic fluids. These model results then are used to reconstruct the environmental conditions associated with cap carbonate deposition and dolomitization in the aftermath of the Marinoan glaciation.

5.1. Primary cap carbonate mineralogy

Three lines of evidence indicate that aragonite was the precursor carbonate mineral for the entire cap carbonate sequence. First, many dolostone units are characterized by $\delta^{44/40}$Ca values that are significantly lower ($\sim<$-1‰) than expected for dolomitized calcite or primary dolomite ($\sim>$-1‰, Gussone et al., 2016; Higgins et al., 2018; Ahm et al., 2018). Second, petrographic observations and sub-sampling of relict aragonite fans (now calcite) from the Hayhook Fm. in Northwest Canada are characterized by low $\delta^{44/40}$Ca values (-2‰) and high Sr/Ca ratios (3–4 mmol/mol, Fig. A.10). Although the micritic matrix has slightly higher $\delta^{44/40}$Ca values (-1.6‰) and lower Sr/Ca ratios (1–2 mmol/mol), the values are still within the range of those expected for neomorphosed aragonite (e.g., Ahm et al., 2018). Relict aragonite fans also are preserved as dolomite in Arctic Alaska and Mongolia (Macdonald et al., 2009; Bold et al., 2016). Third, both limestone and dolomite cap carbonates with elevated Sr/Ca ratios tend to have low $\delta^{44/40}$Ca values (Fig. 8–9), a relationship that is similar to that observed for diagenesis of primary aragonite in the Bahamas (Higgins et al., 2018), and

indistinguishable from the co-variation between $\delta^{44/40}$Ca values and Sr/Ca ratios observed in the aragonite fans and micrite of the Hayhook Fm. (Fig. 5).

5.2. Predictions for diagenesis and fluid flow in the glacial aftermath

Field observations can constrain the timing and relationship between aragonite precipitation, early dolomitization, and Snowball Earth deglaciation. First, the cap dolostone contains wave-generated sedimentary structures indicating that deposition occurred above storm wave-base during the initial kiloyears of sea-level rise (Hoffman et al., 2011; Rose and Maloof, 2010; Macdonald et al., 2013b,a; Hoffman and Macdonald, 2010; Bold et al., 2016). As a result, the chemical composition of the primary sediment likely reflected precipitation from the growing meltwater surface ocean (Shields, 2005; Liu et al., 2014; Yang et al., 2017). Second, the widespread occurrence of temporally coincident early diagenetic cap dolostone units (with consistent covariance between Ca and Mg isotopes) indicate that the primary sediment was dolomitized shortly after deposition during the initial stages of deglaciation. Third, the stratigraphic transition from dolostone to deeper-water limestone suggests a decrease in dolomitization near the time of maximum flooding.

5.2.1. The chemistry of the meltwater lens

The stratigraphic constraints outlined above suggest that the chemistry of the precursor aragonite reflects the chemistry of the meltwater surface ocean. Previous studies have suggested that the meltwater surface ocean was dominated by inputs from the rapid weathering of carbonates in the high $p\mathrm{CO}_2$ glacial aftermath (Hoffman and Schrag, 2002; Higgins and Schrag, 2003).

Chemical weathering of carbonate-dominated terrains produce waters with low $\delta^{44/40}$Ca and δ^{26}Mg values due to the low values of continental carbonates ($\delta^{44/40}$Ca = -1‰, δ^{26}Mg= -2‰). For example, freshwater discharge through carbonate sediments in Florida Bay produce Ca-rich groundwater (Ca^{2+} ~13.5 mmol/kg) with low $\delta^{44/40}$Ca values between -0.4 and -0.9‰. As a result, bulk carbonate sediments in the bay are characterized by $\delta^{44/40}$Ca values down to ~-2‰ (Holmden et al., 2012). In contrast, the concentrations of Mg in groundwater aquifers are orders of magnitudes lower than in seawater (e.g., ~0.6–2 mmol/kg in the Madison aquifer; Jacobson et al., 2010). Mg isotopes in carbonate-dominated groundwater systems are low (~-1.6 and -1.0‰) with travertine deposits recording δ^{26}Mg values down to -4‰ (Tipper et al., 2006; Jacobson et al., 2010). Relict aragonite fans in limestones from the cap carbonate sequence have both $\delta^{44/40}$Ca values and δ^{26}Mg values that approach ~-2‰, consistent with formation in a meltwater surface ocean. Accounting for the fractionation between aragonite and fluid (Gussone et al., 2005; Wang et al., 2013), these measured values predict a meltwater lens with $\delta^{44/40}$Ca values of ~-0.4‰ and δ^{26}Mg values of ~-1‰, similar to the range of observations in the modern settings outlined above (Table 1).

5.2.2. The chemistry of glacial seawater

Widespread dolomitization of aragonite precipitated from a meltwater surface ocean requires a large supply of Mg. Considering the low Mg concentrations of freshwater (see above), we hypothesize that the dolomitizing fluid was glacial seawater. Previous studies have suggested that the chemical composition of glacial seawater was controlled by hydrothermal alteration

of oceanic crust due to a reduction in continental inputs during the global glaciation (Hoffman and Schrag, 2002). As Mg is removed from seawater in both low and high-temperature hydrothermal systems, prolonged global glaciation will tend to lower seawater Mg concentrations relative to ice-free conditions. This mechanism is similar to models for the near continent free Archean (Jones et al., 2015). As a result, Mg/Ca ratios in glacial seawater are expected to be lower in comparison with Cenozoic seawater ratios, although still substantially higher than ratios expected for freshwaters (see above), and lower than the general conditions thought to characterize the Proterozoic (Jones et al., 2015). Similarly, a reduction in carbonate burial, increase in seafloor dissolution (Hoffman and Schrag, 2002), and continued high-temperature hydrothermal alteration are expected to have raised Ca concentrations and lowered $\delta^{44/40}$Ca values relative to pre-glacial seawater. Given these assumptions, we expect that glacial seawater was characterized by relatively low Mg/Ca ratios, low $\delta^{44/40}$Ca values, and high δ^{26}Mg values (Table 1).

5.2.3. Fluid circulation in platform sediments during the glacial aftermath

Deglaciation and meltwater discharge in coastal zones provides a physical mechanism to circulate seawater through carbonate platforms worldwide (Fig. 7). During the development of an expansive meltwater wedge in coastal areas, density gradients between meltwater and glacial seawater promote buoyant convection of fluids within platform sediments (Wilson, 2005; Cooper et al., 1964; Reilly and Goodman, 1985). The less dense meltwater forms a wedge and flows seawards to displace more dense seawater (Fig. 7A). In the transition zone between meltwater and seawater, seawater is diluted

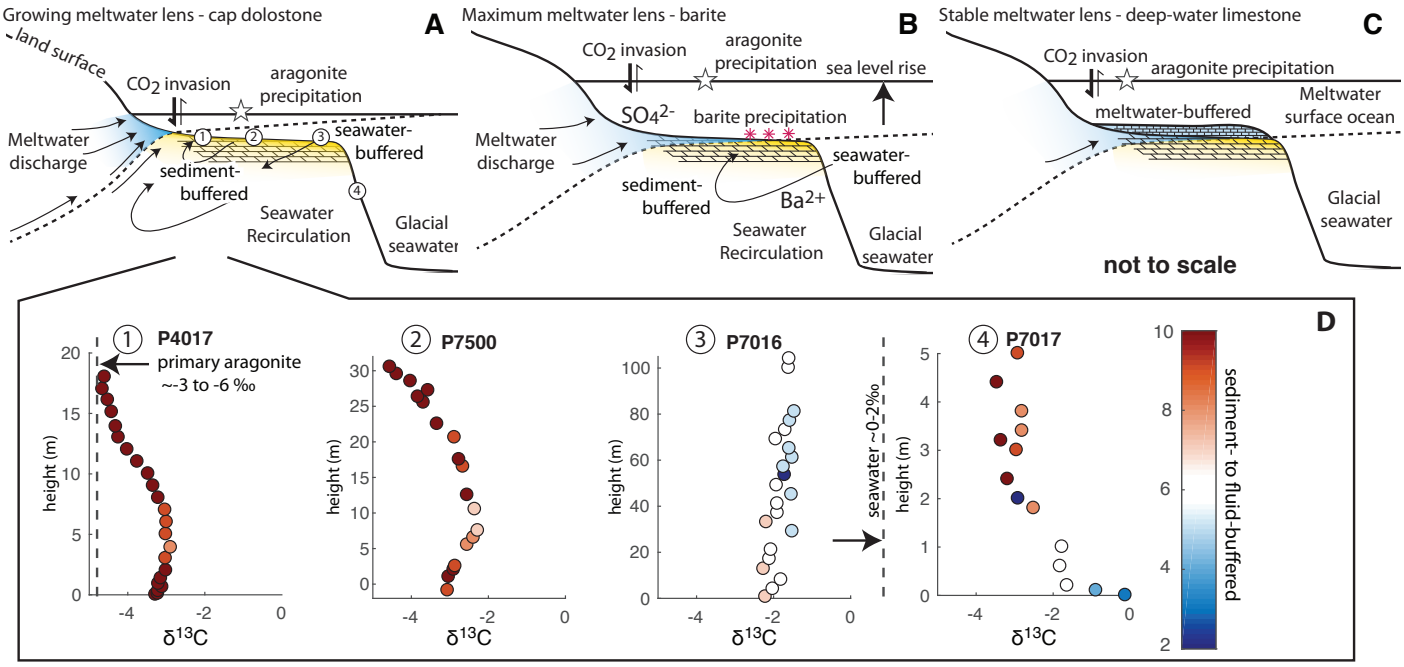

Figure 7: **Fluid flow during deglaciation** Schematic representation of fluid circulation in platform sediments during deglaciation (A) High rates of meltwater discharge from land based ice sheets in the initial stages of deglaciation drives seawater recirculation and dolomitization of primary aragonite in platform environments worldwide. (B) As the meltwater lens reaches its maximum extent, barite precipitates at the interface between meltwater and seawater (dashed line illustrates boundary between meltwater and seawater). (C) While aragonite is continuously precipitating in the surface ocean, dolomitization ceases and is replaced by aragonite neomorphism to calcite as the meltwater lens covers the platform and infiltrates the pore space. (D) Keilberg cap dolostone units from the Congo Craton shown in their relative position across the margin from the inner-most platform environment (P4017) to the foreslope (P7017). δ^{13}C values are colored by diagenetic model results of the degree of fluid- versus sediment-buffered dolomitization (on a scale from 0–10 with 10 being the most sediment-buffered), corresponding to the flow path of seawater recirculation through the platform.

and entrained in the upward flow of freshwater through turbulent mixing (Cooper et al., 1964). To compensate the seaward flow of diluted waters, seawater flows landward from the edge of the platform, establishing convective circulation (Fig. 7). This type of seawater recirculation has been recognized in modern coastal systems (Wilson, 2005), and hypothesized to play an important role in the dolomitization of modern shallow-water carbonate sediments (Vahrenkamp and Swart, 1994).

Seawater recirculation depends on the rate of meltwater discharge at the surface (Cooper et al., 1964; Reilly and Goodman, 1985) and will be most vigorous during ice sheet melting. In addition, seawater recirculation is expected to result in longer fluid-flow paths for sites on the inner-most platform and shorter fluid-flow paths on the platform edge (Fig. 7). In the context of the cap dolostone, this type of circulation would result in seawater-buffered dolomites on the platform edge and sediment-buffered dolomites on the inner platform – exactly the spatial pattern observed in the cap dolostone units in Namibia (Fig. 7D). Deeper distal environments will be exposed to less fluid flow because rates of seawater recirculation decline with distance from the freshwater-seawater interface (Cooper et al., 1964; Reilly and Goodman, 1985). As a result, more sediment-buffered carbonates are expected in deeper foreslope settings, consistent with observations from basinal sections in Death Valley (F1340) and Namibia (P7017).

In sections more proximal to land-based ice-sheets, continued meltwater discharge through sediments would result in meteoric-style diagenesis (Fig. 7). This type of diagenesis is consistent with observations from limestones in South Australia (C213) and Kalahari (F817) deposited prior to maximum

deglacial flooding. In addition to the lack of dolomite, the observations of very low δ^{26}Mg values (down to -4‰) and relatively high $\delta^{44/40}$Ca values (up to ∼-0.6‰) in these cap carbonates are consistent with alteration in meltwater-dominated diagenetic fluids. During deglaciation, the growth of the meltwater surface ocean may lead to stratigraphic changes in the style of diagenetic alteration. Sites where diagenesis initially is dominated by circulation of glacial seawater may transition to meltwater-dominated as the thickness of the meltwater surface ocean increases (Fig. 7C). A reduction in seawater recirculation and a shift to a more meltwater-dominated fluid with time provides an explanation for the stratigraphic transition from a transgressive cap dolostone to a deep-water limestone in multiple sections (e.g., the Maieberg Fm. in Namibia and Hayhook Fm. in Northwest Canada, Fig. 7C). In these limestone units, relatively high $\delta^{44/40}$Ca values (up to ∼-0.8‰) and low δ^{26}Mg values (down to ∼-3‰) are consistent with alteration in the meltwater lens (e.g., J1132, P4017, Fig. 8).

5.2.4. Barite precipitation

One of the most enigmatic characteristics of the Marinoan cap carbonate sequence is the widespread observation of seafloor barite ($BaSO_4$) at the transition between the cap dolostone and the deep-water limestone (e.g., Crockford et al., 2017). This barite hosts unique Δ^{17}O anomalies that indicate high CO_2/O_2 ratios in the aftermath of the global glaciation and require that SO_4^{2-} incorporated into barite was in communication with the atmosphere prior to its incorporation (Bao et al., 2008). We propose that discharge of meltwater provided SO_4^{2-} from continental weathering of sulfides (Hoffman et al., 2011; Crockford et al., 2016) while the circulation of

anoxic glacial seawater through sediments in the glacial aftermath provided a source of Ba^{2+} (Hoffman et al., 2011). This mechanism links the mineralogical transition from dolostone to limestone and the formation of barite to the existence of an interface between the meltwater lens and glacial seawater (Fig. 7B).

5.3. Modeling cap carbonate dolomitization and aragonite neomorphism

To test whether the assumptions used to construct our model for cap carbonate deposition and dolomitization are consistent with the observed geochemical variability, we evaluate each dataset using a model of carbonate diagenesis (Ahm et al., 2018). First, the model is used to constrain the composition of the meltwater lens by simulating neomorphism of primary aragonite in meltwater (based on the concept in Fig. 7). Model results for the meltwater lens are estimated from measurements of $\delta^{44/40}$Ca values, δ^{26}Mg values, and Sr/Ca ratios from cap limestone units. Second, the model is used to constrain the composition of glacial seawater by simulating early marine dolomitization. Model results for glacial seawater are estimated from measurements of $\delta^{44/40}$Ca values, δ^{26}Mg values, and Sr/Ca ratios from the cap dolostone units. Using model results for both dolomitization and neomorphism, we estimate the composition of the primary aragonite and use these constrains to evaluate the origin and variability in δ^{13}C values recorded in cap carbonates worldwide (Table 1).

5.3.1. Aragonite neomorphism in the meltwater lens

A subset of cap carbonate samples from South Australia, Death Valley, Congo, Kalahari, and Northwest Canada are limestone. On the Namibian

Table 1: Summary of expectations and model results (see Appendix C for sensitivity tests of model optimization results).

Variable	Meltwater	Seawater	Primary Aragonite
Expectations:			
$\delta^{44/40}$Ca	-0.4 to -0.9‰	<0‰	<-1.6‰
δ^{26}Mg	<-1‰	>-0.8‰	<-1‰
Mg/Ca	<0.15 mol/mol	<5 mol/mol	∼10 mmol/mol
Model fit:			
$\delta^{44/40}$Ca	-0.4‰	-0.6‰	-2.1‰
δ^{26}Mg	-1.8‰	-0.2‰	-2 to -1‰
Mg/Ca (mmol/mol)	0.025	0.9	20
δ^{13}C	-11‰	0 to +2‰	-6 to -3‰

margin of the Congo craton and in northwestern Canada, deep-water limestones overlie a transgressive cap dolostone unit, but in South Australia, Death Valley, and Kalahari the limestones locally are deposited below the surface of maximum flooding. These limestone units are geochemically distinct from the cap dolostones with low δ^{13}C values, high $\delta^{44/40}$Ca values, and low δ^{26}Mg values (Fig. 8). The most fluid-buffered samples are from South Australia (C213) and record low δ^{26}Mg values (∼-4‰), relatively high $\delta^{44/40}$Ca values (∼-0.7‰), and low δ^{13}C values (∼-7‰, Fig. 3). In contrast, the most sediment-buffered samples are from limestones from a foreslope succession in Death Valley (F1340) that record high δ^{26}Mg values (∼-1‰), low $\delta^{44/40}$Ca values (∼-1.9‰), and intermediate δ^{13}C values (∼-3‰, Fig. 4).

The model fit to the geochemical data from these limestone sections yields a diagenetic fluid with a relatively low $\delta^{44/40}$Ca value (∼-0.4‰), a very low δ^{26}Mg value (∼-1.8‰), a very low δ^{13}C value (∼-11‰, Fig. 8), and a very low Mg/Ca ratio (∼0.025 mol/mol, Table 1). The range in the geochemical

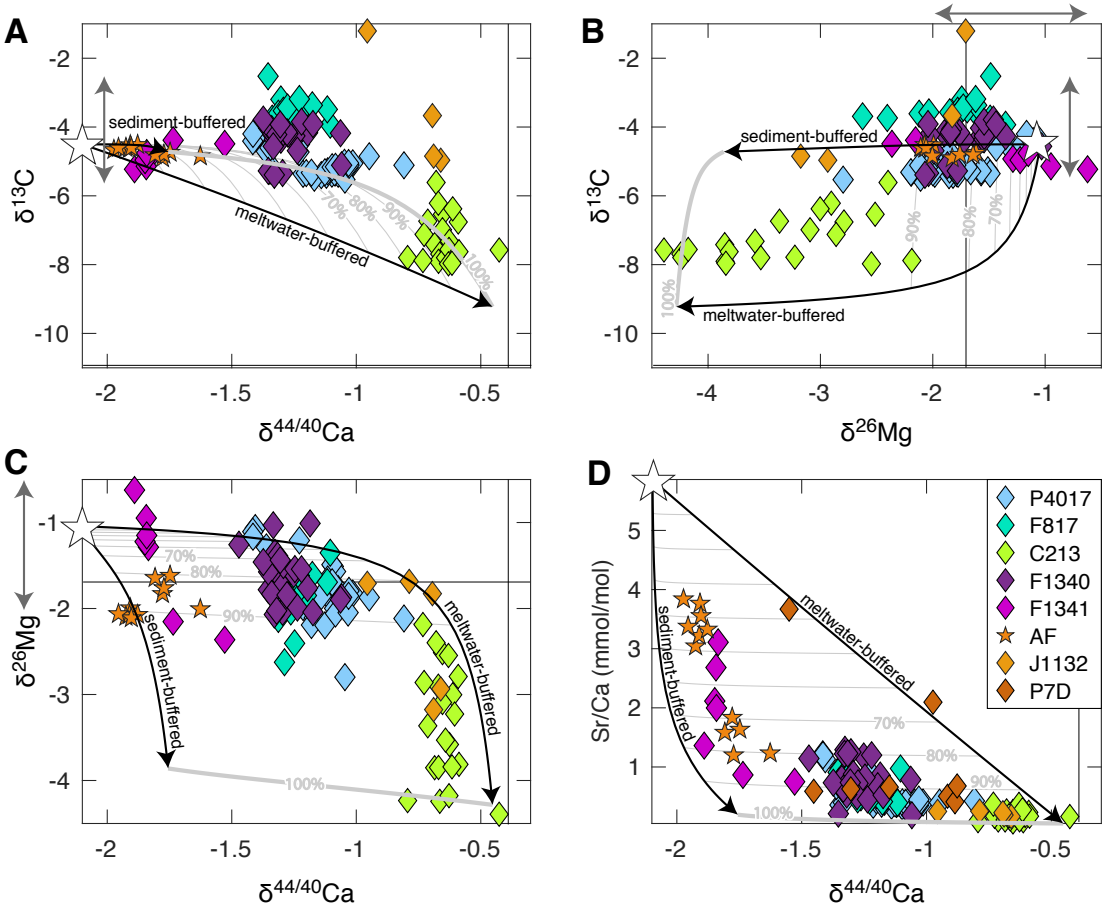

Figure 8: **Meltwater diagenesis** Modeling results for neomorphism of primary aragonite (white star) in the meltwater lens (thin black grid lines). The initial composition of aragonite likely varied across the platform (small grey arrow). The two black arrows indicate the two end-member diagenetic pathways for neomorphism in either fully fluid- or sediment-buffered conditions. The grey lines of the model phase-space indicate the degree of neomorphism in the meltwater lens (from 0–100%). Model results are compared to measurements from cap limestones from Namibia (blue), Kalahari (cyan), Australia (green), Death Valley (purple/pink), and Northwest Canada (yellow). These measurements span the range between the fluid- and sediment-buffered model trajectories and the primary mineral. (A) δ^{13}C versus $\delta^{44/40}$Ca values, (B) δ^{13}C versus δ^{26}Mg values, (C) δ^{26}Mg versus $\delta^{44/40}$Ca values, and (D) Sr/Ca ratios versus $\delta^{44/40}$Ca values. Sample color code and legend correspond to Figs. 1–6.

data suggests that the chemistry of the meltwater lens was somewhat variable across different continental margins (Fig. 8), consistent with expectations of the chemistry of a meltwater surface ocean in the aftermath of a global glaciation (section 5.2.1).

5.3.2. Early marine dolomitization

Cap dolostone samples from South Australia, Congo, Kalahari, Death Valley, Northwest Canada, and Arctic Alaska have geochemical signatures consistent with early marine dolomitization by a seawater-like fluid (Fig. 9). The most fluid-buffered samples come from platform margin to upper slope settings on the Congo Craton and in South Australia (C215, P7016, Fig. 2–3) with high $\delta^{44/40}$Ca values (∼-0.6‰), low δ^{26}Mg values (∼-2.2‰), and high δ^{13}C values (∼+2‰). The most sediment-buffered samples come from the innermost platform and deeper foreslope settings of the Congo Craton, and foreslope settings in Death Valley (P4017, P7500, F1340, Fig. 2–4) with low $\delta^{44/40}$Ca values (∼-1.5‰), high δ^{26}Mg values (∼-1‰), and relatively low δ^{13}C values (∼-5‰).

The model fit to the geochemical data from these cap dolostone units (Fig. 9) indicate that the dolomitizing fluid had a $\delta^{44/40}$Ca value of ∼-0.4‰, a δ^{26}Mg value ∼-0.2‰, a Mg/Ca ratio of ∼0.9 mol/mol, and a δ^{13}C value of ∼2‰ (Table 1). However, when excluding a particular section in Australia (C215) with higher δ^{13}C values than observed elsewhere, the model fit to the geochemical data yields a δ^{13}C value of ∼0‰ for the dolomitizing fluid. In general, these model estimates are consistent with our expectations for the chemistry of seawater in the wake of a prolonged global glaciation where the composition of seawater is set by hydrothermal circulation (section

5.2.2, Hoffman and Schrag, 2002; Jones et al., 2015). The model estimate of relatively high $\delta^{44/40}$Ca values of the dolomitizing fluid provide further evidence that the dolomitizing occurred during early marine diagenesis in relatively unaltered seawater as crustal fluids would be expected to have lower $\delta^{44/40}$Ca value due to reactions with the wall rock. These model results suggest that the system can be well-represented by a single fluid-buffered end-member for seawater rather than multiple end-members. These results do not imply that smaller scale geochemical variability did not exist during and immediately after deposition of the cap carbonate, but does not support the existence of end-members that are far outside the range of the model phase-space. It is therefore not necessary to change the chemistry of seawater over time to explain the global stratigraphic variability in the geochemistry of basal Ediacaran cap dolostones.

5.3.3. The chemistry of primary aragonite

Model results also can be used to estimate the chemical and isotopic composition of the primary carbonate sediment. The model results outlined above are consistent with primary aragonite with a low $\delta^{44/40}$Ca value (∼-2.1‰) and relatively high δ^{26}Mg values (between ∼-1 and -2‰, Table 1, Fig. 8–9). The large range in δ^{26}Mg values in the primary sediment may reflect either a small degree of mixing between Mg-poor meltwater and Mg-rich seawater across the continental margin or small contributions from dolomite in the bulk sample.

The best model fit to the global dataset indicates that the primary aragonite was characterized by δ^{13}C values ∼-5‰ with some variability across continents (between ∼-6 to -3‰, Figs. 8–9). This aragonite subsequently

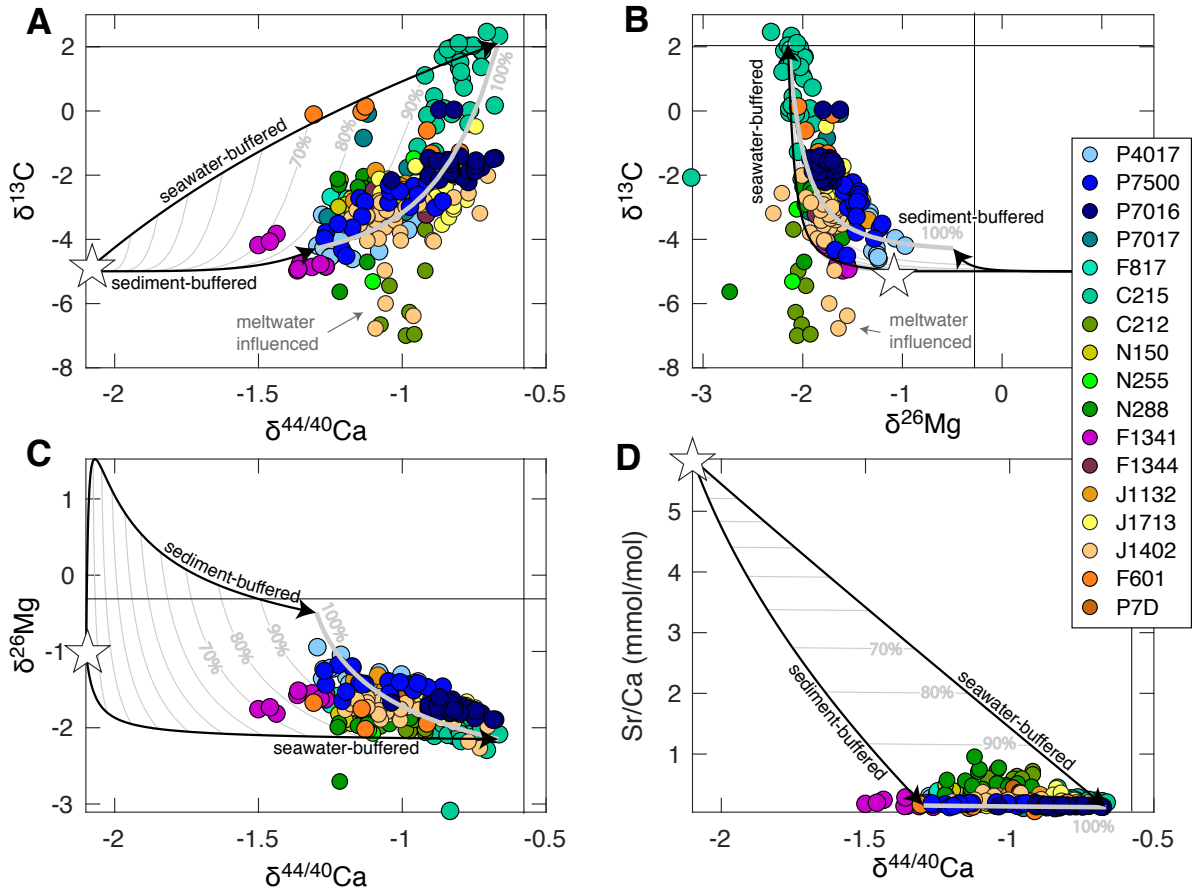

Figure 9: **Seawater dolomitization** Modeling results for dolomitization of primary aragonite (white star) in glacial seawater (thin black grid lines). The two black arrows indicate the two end-member diagenetic pathways for dolomitization in either fully fluid- or sediment-buffered conditions. The grey lines on the model phase-space indicate the degree of dolomitization (from 0–100%). Grey arrows and text indicate samples that are interpreted to also be influenced by diagenesis in the meltwater surface ocean (see also Fig. 8). Model results are compared to measurements of cap dolostones from Namibia (blue), Australia (green), Death Valley (pink), Northwest Canada (yellow), and Arctic Alaska (orange). These measurements span the range between the fluid- and sediment-buffered model trajectories. (A) δ^{13}C versus $\delta^{44/40}$Ca values, (B) δ^{13}C versus δ^{26}Mg values, (C) δ^{26}Mg versus $\delta^{44/40}$Ca values, and (D) Sr/Ca ratios versus $\delta^{44/40}$Ca values. Sample color code and legend correspond to Figs. 1–6.

was dolomitized in glacial seawater with a δ^{13}C value between ∼0–2‰. Samples that were dolomitized in fluid-buffered settings were reset toward the composition of glacial seawater (e.g., P7016, C215), whereas samples that were dolomitized in more sediment-buffered settings retained some of the chemical signatures of the primary aragonite (e.g., P7500, P4017). Samples that avoided early dolomitization entirely were neomorphosed to low-Mg calcite during diagenesis in the expansive meltwater surface ocean and reflect its low δ^{13}C value (e.g., Maieberg Fm. limestones).

5.4. Carbon isotope excursions in cap carbonates

According to our model, the large range in δ^{13}C values recorded in cap carbonate deposits worldwide is the consequence of different styles of early diagenesis and fluid flow in platform environments during the glacial aftermath. Model results and measurements of relict aragonite fans suggest that the precursor sediment had low but somewhat variable δ^{13}C values (between -3 to -6‰, Fig. 8) – a result that is further corroborated by model results of diagenesis in the meltwater surface ocean (down to -11‰).

Two mechanisms may explain these low $\delta^{13}C_{DIC}$ values in the meltwater surface ocean. First, low $\delta^{13}C_{DIC}$ values are observed in modern coastal systems associated with large fluxes of respired organic matter (Patterson and Walter, 1994). For example, in Florida Bay high rates of submarine groundwater discharge contribute to coastal waters with $\delta^{13}C_{DIC}$ values down to ∼-7‰, likely due to the addition of respired organic matter from the Florida Everglades (Patterson and Walter, 1994). To invoke this mechanism and explain the low $\delta^{13}C_{DIC}$ values in the meltwater lens requires a large terrestrial biosphere (e.g., Knauth and Kennedy, 2009) or elevated rates of

organic carbon oxidation in the underlying sediments.

Alternatively, low $\delta^{13}C_{DIC}$ values in shallow-water aragonite producing environments may result from kinetic isotope effects due to CO_2 invasion in a poorly-buffered meltwater surface ocean (Baertschi, 1952; Lazar and Erez, 1992). Hydration and/or hydroxylation of CO_2 is associated with a large kinetic isotope effect (estimates between $\sim$-11 to -39‰, Zeebe and Wolf-Gladrow, 2001) and continued invasion of CO_2 into surface waters can result in local $\delta^{13}C_{DIC}$ values below -10‰ (Lazar and Erez, 1992). Disequilibrium effects are expressed in modern settings where extremely low $\delta^{13}C_{DIC}$ values are observed during rapid precipitation of carbonates in high alkalinity waters (e.g., Falk et al., 2016) and/or during high sustained rates of biological productivity in both freshwater (Herczeg and Fairbanks, 1987) and marine environments (Lazar and Erez, 1992). Enhanced nutrient inputs during the intense weathering associated with the post-glacial hothouse (Kunzmann et al., 2013) together with the relatively low buffering capacity of a meltwater surface ocean provide a plausible mechanism to explain the increase in local biological productivity required to produce significant disequilibrium between the meltwater surface ocean and the atmosphere.

Given the important role of photosynthetic microbial mat communities in driving carbon isotopic disequilibrium in modern evaporation pans and sedimentological observations of anomalous 'tubestone' stromatolitic units in the cap carbonate sequence (e.g., Fig. 2, 4, 5; Hoffman et al., 2011), we hypothesize that microbial mats played an important role in driving isotopic disequilibrium in the meltwater surface ocean. The rates of primary production required to drive disequilibrium in both saline microbial mat systems

and freshwater lakes are ∼30 mmol m^{-2} d^{-1} (Herczeg and Fairbanks, 1987; Lazar and Erez, 1992), well within the range of estimates for productivity in the modern surface ocean. This hypothesis is not inconsistent with the low organic carbon content in the cap carbonate sequences. While it is generally agreed that microbial mats were likely organic-rich at the sediment-water interface, these same deposits are rarely associated with high concentrations of organic matter in the rock record. In addition, high carbonate precipitation rates may have locally masked organic carbon burial in these sediments. Finally, in addition to providing an explanation for low $\delta^{13}C_{DIC}$, productivity-driven disequilibrium may provide insights into the anomalous sedimentary fabrics associated with cap carbonates as disequilibrium in the carbonate system is expected to lead to high degrees of carbonate supersaturation.

According to this hypothesis, the persistence of low $\delta^{13}C_{DIC}$ values through the cap carbonate sequence above the dolostone units reflect extended periods of disequilibrium between the atmosphere and meltwater surface ocean through the time interval of maximum flooding (Fig. 7C). Periods of disequilibrium were likely driven by algal blooms, resulting in precipitation of aragonite in the less buffered meltwater ocean during times of CO_2 invasion. Isotopically depleted crystal fans in deeper-water facies also suggest that these conditions extended to over-deepened shelves and slopes, consistent with the development of a thick meltwater surface ocean (∼1 km, Yang et al., 2017) with a duration of $10^4 - 10^5$ years. Due to the decrease in fluid-flow in sediments in deeper-waters, the accumulation of carbonate sediments in deep underfilled basins limited the extent of fluid-buffered alteration and preserved platform top $\delta^{13}C_{DIC}$ values. These results suggest that the

stratigraphic variability of δ^{13}C values in the cap carbonate sequence is a product of different styles of diagenesis/dolomitization of primary aragonite. This model explains the regional and stratigraphic variability in terms of mixing between sediment-buffered neomorphosmed aragonite and both sediment- and fluid-buffered dolomite formed from the dolomitization of aragonite with glacial seawater.

Measurements and diagenetic model results of cap dolostone dolomitization suggest that the $\delta^{13}C_{DIC}$ values of glacial seawater sourced from intermediate water depths was ∼0–2‰ (Fig. 9A). As the $\delta^{13}C_{DIC}$ value of glacial seawater would depend on the initial δ^{13}C of the ocean-atmosphere system, the partitioning of CO_2 between ocean and atmosphere, and temperature-dependent fractionation between the inorganic carbon species, $\delta^{13}C_{DIC}$ values near 0‰ are consistent with expectations for glacial seawater (Higgins and Schrag, 2003).

6. Conclusion

- Systematic covariation between Ca and Mg isotope values in more than 20 cap dolostone sections indicate that the dolomite is not a primary precipitate, and instead is the product of secondary early dolomitization of calcium carbonate.

- The low Ca isotope values (below -1.1‰) of cap dolomites and the covariation between Ca isotope values and Sr/Ca ratios in the cap limestones indicate that the precursor mineralogy was aragonite.

- Results from diagenetic modeling suggest that primary aragonite was

deposited in the meltwater surface ocean with low $\delta^{13}C_{DIC}$ values (down to ∼-11‰).

- $\delta^{13}C$ values of the meltwater surface ocean were low due to either high rates of organic matter remineralization in glacial groundwater or kinetic isotope effects caused by CO_2 invasion from the atmosphere into the surface ocean. Importantly, these values do not directly reflect secular variations in the DIC.

- Dolomitization of platform sediments is consistent with fluid flow and seawater recirculation during global deglaciation.

- Platform sediments were dolomitized during sea-level rise in glacial seawater with low Mg/Ca ratios (∼0.1), low Ca isotope values (∼-0.6‰), high Mg isotope values (-0.2‰), and $\delta^{13}C_{DIC}$ values of ∼0–2‰.

7. Acknowledgments

ASCA acknowledges support from The Carlsberg Foundation. JAH acknowledges support from NSF grant no. IES1410317 and from NSF OCE CAREER Grant No. 1654571. ASA and CJB acknowledges support from the Danish National Research Foundation (Grant No. DNRF53). We would like to thank Nicolas Slater for assistance in the lab and we thank Clara Blättler, Peter Crockford, and Blake Dyer for insightful discussions. Finally, we thank three anonymous reviewers and the editor for constructive comments that significantly improved this manuscript.

References

Ahm, A-S. C., Bjerrum, C. J., Blättler, C. L., Swart, P. K., Higgins, J. A., 2018. Quantifying early marine diagenesis in shallow-water carbonate sediments. Geochimica et Cosmochimica Acta 236, 140–159. https://doi.org/10.1016/j.gca.2018.02.042

Baertschi, P., 1952. Die fraktionierung der kohlenstoffisotopen bei der absorption von kohlendioxyd. Helvetica Chimica Acta 35 (3), 1030–1036. http://dx.doi.org/10.1038/168288a0

Bao, H., Lyons, J. R., Zhou, C., 2008. Triple oxygen isotope evidence for elevated CO_2 levels after a Neoproterozoic glaciation. Nature 453, 504–506. http://dx.doi.org/10.1038/nature06959

Blättler, C. L., Higgins, J. A., 2017. Testing Urey's carbonate-silicate cycle using the calcium isotopic composition of sedimentary carbonates. Earth and Planetary Science Letters 479, 241–251. https://dx.doi.org/10.1016/j.epsl.2017.09.033

Blättler, C. L., Miller, N. R., Higgins, J. A., 2015. Mg and Ca isotope signatures of authigenic dolomite in siliceous deep-sea sediments. Earth and Planetary Science Letters 419 (0), 32–42. http://dx.doi.org/10.1016/j.epsl.2015.03.006

Bold, U., Smith, E. F., Rooney, A. D., Bowring, S. A., Buchwaldt, R., Dudás, F. Ö., Ramezani, J., Crowley, J. L., Schrag, D. P., Macdonald, F. A., 2016. Neoproterozoic stratigraphy of the Zavkhan terrane of Mongolia: the backbone for Cryogenian and early Ediacaran

735 chemostratigraphic records. American Journal of Science 316, 1–63.
736 https://dx.doi.org/10.2475/01.2016.01

737 Cooper, H. H., Kohout, F. A., Henry, H. R., Glover, R. E., 1964. Sea water
738 in coastal aquifers. U.S. Geol. Surv. Water-supply Pap. (1613-C), 84.

739 Crockford, P. W., Cowie, B. R., Johnston, D. T., Hoffman, P. F., Sugiyama,
740 I., Pellerin, A., Bui, T. H., Hayles, J., Halverson, G. P., Macdonald, F. A.,
741 Wing, B. A., 2016. Triple oxygen and multiple sulfur isotope constraints
742 on the evolution of the post-Marinoan sulfur cycle. Earth and Planetary
743 Science Letters 435, 74–83. https://doi.org/10.1016/j.epsl.2015.12.017

744 Crockford, P. W., Hodgskiss, M. S., Uhlein, G. J., Caxito, F.,
745 Hayles, J. A., Halverson, G. P., 2017. Linking paleocontinents
746 through triple oxygen isotope anomalies. Geology 46 (2), 179–182.
747 http://dx.doi.org/10.1130/G39470.1

748 Fabre, S., Berger, G., Chavagnac, V., Besson, P., 2013. Origin of cap car-
749 bonates: An experimental approach. Palaeogeography, Palaeoclimatology,
750 Palaeoecology 392, 524–533. https://doi.org/10.1016/j.palaeo.2013.10.006

751 Falk, E. S., Guo, W., Paukert, A. N., Matter, J. M., Mervine, E. M.,
752 Kelemen, P. B., 2016. Controls on the stable isotope compositions of
753 travertine from hyperalkaline springs in Oman: Insights from clumped
754 isotope measurements. Geochimica et Cosmochimica Acta 192, 1–28.
755 https://doi.org/10.1016/j.gca.2016.06.026

756 Fantle, M. S., DePaolo, D. J., 2007. Ca isotopes in carbonate sedi-
757 ment and pore fluid from ODP Site 807A: The Ca^{2+}(aq)–calcite equi-

librium fractionation factor and calcite recrystallization rates in Pleistocene sediments. Geochimica et Cosmochimica Acta 71 (10), 2524–2546. http://dx.doi.org/10.1016/j.gca.2007.03.006

Fantle, M. S., Higgins, J., 2014. The effects of diagenesis and dolomitization on Ca and Mg isotopes in marine platform carbonates: Implications for the geochemical cycles of Ca and Mg. Geochimica et Cosmochimica Acta 142, 458–481. http://dx.doi.org/10.1016/j.gca.2014.07.025

Gammon, P. R., 2012. An organodiagenetic model for Marinoan-age cap carbonates. Sedimentary Geology 243-244, 17–32. https://doi.org/10.1016/j.sedgeo.2011.12.004

Gammon, P. R., McKirdy, D. M., Smith, H. D., 2012. The paragenetic history of a Marinoan cap carbonate. Sedimentary Geology 243-244, 1–16. https://doi.org/10.1016/j.sedgeo.2011.07.004

Grotzinger, J. P., Knoll, A. H., 1995. Anomalous Carbonate Precipitates: Is the Precambrian the Key to the Permian? Palaios 10 (6), 578–596. https://dx.doi.org/10.2307/3515096

Gussone, N., Böhm, F., Eisenhauer, A., Dietzel, M., Heuser, A., Teichert, B. M. A., Reitner, J., Wörheide, G., Dullo, W-C., 2005. Calcium isotope fractionation in calcite and aragonite. Geochimica et Cosmochimica Acta 69 (18), 4485–4494. http://dx.doi.org/10.1016/j.gca.2005.06.003

Gussone, N., Dietzel, M., 2016. Calcium Isotope Fractionation During Mineral Precipitation from Aqueous Solution in: Calcium Stable Isotope Geo-

chemistry. Advances in Isotope Geochemistry. Springer, Berlin, Heidelberg https://doi.org/10.1007/978-3-540-68953-9_3

Herczeg, A. L., Fairbanks, R. G., 1987. Anomalous carbon isotope fractionation between atmospheric CO_2 and dissolved inorganic carbon induced by intense photosynthesis. Geochimica et Cosmochimica Acta 51 (4), 895–899. http://dx.doi.org/10.1016/0016-7037(87)90102-5

Henderson, G. M., Slowey, N. C., Haddad, G. A., 1999. Fluid flow through carbonate platforms: constraints from $^{234}U/^{238}U$ and Cl^- in Bahamas pore-waters. Earth and Planetary Science Letters 169 (1–2), 99–111. http://dx.doi.org/10.1016/S0012-821X(99)00065-5

Higgins, J. A., Blättler, C. L., Lundstrom, E. A., Santiago-Ramos, D., Akhtar, A., Ahm, A-S. C., Bialik, O., Holmden, C., Bradbury, H., Murray, S. T., Swart, P., 2018. Mineralogy, early marine diagenesis, and the chemistry of shallow water carbonate sediments. Geochimica et Cosmochimica Acta 220, 512–534. https://doi.org/10.1016/j.gca.2017.09.046

Higgins, J. A., Schrag, D. P., 2003. Aftermath of a snowball Earth. Geochemistry, Geophysics, Geosystems 4 (3). http://dx.doi.org/10.1029/2002GC000403

Higgins, J. A., Schrag, D. P., 2010. Constraining magnesium cycling in marine sediments using magnesium isotopes. Geochimica et Cosmochimica Acta 74 (17), 5039–5053. http://dx.doi.org/10.1016/j.gca.2010.05.019

Hoffman, P. F., 2011. Strange bedfellows: glacial diamictite and cap carbon-

ate from the Marinoan (635 Ma) glaciation in Namibia. Sedimentology 58 (1), 57–119. http://dx.doi.org/10.1111/j.1365-3091.2010.01206.x

Hoffman, P. F., Halverson, G. P., Domack, E. W., Husson, J. M., Higgins, J. A., Schrag, D. P., 2007. Are basal Ediacaran (635 Ma) post-glacial "cap dolostones" diachronous? Earth and Planetary Science Letters 258 (1–2), 114–131. http://dx.doi.org/10.1016/j.epsl.2007.03.032

Hoffman, P. F., Kaufman, A. J., Halverson, G. P., Schrag, D. P., 1998. A Neoproterozoic Snowball Earth. Science 281 (5381), 1342–1346. http://dx.doi.org/10.1126/science.281.5381.1342

Hoffman, P. F., Macdonald, F. A., 2010. Sheet-crack cements and early regression in Marinoan (635 Ma) cap dolostones: Regional benchmarks of vanishing ice-sheets? Earth and Planetary Science Letters 300 (374-384). https://dx.doi.org/10.1016/j.epsl.2010.10.027

Hoffman, P. F., Macdonald, F. A., Halverson, G. P., 2011. Chemical sediments associated with Neoproterozoic glaciation: iron formation, cap carbonate, barite and phosphorite. Geological Society, London, Memoirs 36 (1), 67–80. http://dx.doi.org/10.1111/j.1365-3091.2010.01206.x

Hoffman, P. F., Schrag, D. P., 2002. The Snowball Earth hypothesis: testing the limits of global change. Terra Nova 14 (3), 129–155. http://dx.doi.org/10.1046/j.1365-3121.2002.00408.x

Holmden, C., Papanastassiou, D. A., Blanchon, P., Evans, S., 2012. $\delta^{44/40}$Ca variability in shallow water carbonates and the impact of submarine groundwater discharge on Ca-cycling in ma-

825 rine environments. Geochimica et Cosmochimica Acta 83, 179–194.
826 https://doi.org/10.1016/j.gca.2011.12.031

827 Husson, J. M., Higgins, J. A., Maloof, A. C., Schoene, B., 2015.
828 Ca and Mg isotope constraints on the origin of Earth's deepest
829 C excursion. Geochimica et Cosmochimica Acta 160 (0), 243–266.
830 http://dx.doi.org/10.1016/j.gca.2015.03.012

831 Jacobson, A. D., Holmden, C., 2008. δ^{44}Ca evolution in a carbonate
832 aquifer and its bearing on the equilibrium isotope fractionation factor
833 for calcite. Earth and Planetary Science Letters 270 (3–4), 349–353.
834 http://dx.doi.org/10.1016/j.epsl.2008.03.039

835 Jacobson, A. D., Zhang, Z., Lundstrom, C., Huang, F., 2010. Behav-
836 ior of Mg isotopes during dedolomitization in the madison aquifer,
837 South Dakota. Earth and Planetary Science Letters 297 (3), 446–452.
838 https://doi.org/10.1016/j.epsl.2010.06.038

839 Jiang, G., Kennedy, M. J., Christie-Blick, N., 2003. Stable isotopic evidence
840 for methane seeps in Neoproterozoic postglacial cap carbonates. Nature
841 426, 822–826. http://dx.doi.org/10.1038/nature02201

842 Jones, C., Nomosatryo, S., Crowe, S. A., Bjerrum, C. J., Canfield, D. E.,
843 2015. Iron oxides, divalent cations, silica, and the early earth phosphorus
844 crisis. Geology 43 (2), 135-138. https://doi.org/10.1130/G36044.1

845 Kasemann, S. A., Hawkesworth, C. J., Prave, A. R., Fallick, A. E., Pear-
846 son, P. N., 2005. Boron and calcium isotope composition in Neopro-
847 terozoic carbonate rocks from Namibia: evidence for extreme environ-

mental change. Earth and Planetary Science Letters 231 (1–2), 73–86. http://dx.doi.org/10.1016/j.epsl.2004.12.006

Kasemann, S. A., Pogge von Strandmann, P. A. E., Prave, A. R., Fallick, A. E., Elliott, T., Hoffmann, K.-H., 2014. Continental weathering following a Cryogenian glaciation: Evidence from calcium and magnesium isotopes. Earth and Planetary Science Letters 396, 66–77. http://dx.doi.org/10.1016/j.epsl.2014.03.048

Kennedy, M. J., 1996. Stratigraphy, sedimentology, and isotopic geochemistry of Australian Neoproterozoic postglacial cap dolostones; deglaciation, δ^{13}C excursions, and carbonate precipitation. Journal of Sedimentary Research 66 (6), 1050–1064. http://dx.doi.org/10.2110/jsr.66.1050

Kennedy, M. J., Christie-Blick, N., Sohl, L. E., 2001. Are Proterozoic cap carbonates and isotopic excursions a record of gas hydrate destabilization following Earth's coldest intervals? Geology 29 (5), 443–446. https://doi.org/10.1130/0091-7613(2001)029<0443:APCCAI>2.0.CO;2

Kirschvink, J. L., 1992. Late Proterozoic Low-Latitude Global Glaciation: the Snowball Earth. The Proterozoic biosphere: a multidisciplinary study. Cambridge University Press.

Knauth, L. P., Kennedy, M. J., 2009. The late Precambrian greening of the Earth. Nature 460 (7256), 728–732. http://dx.doi.org/10.1038/nature08213

Knoll, A. H., Walter, M., Narbonne, G. M., Christie-Blick, N., 2006. The

870 Ediacaran Period: a new addition to the geologic time scale. Lethaia 39
871 (1), 13–30. http://dx.doi.org/10.1080/00241160500409223

872 Komar, N., Zeebe, R. E., 2016. Calcium and calcium isotope changes during
873 carbon cycle perturbations at the end-Permian. Paleoceanography 31 (1),
874 115–130. https://doi.org/10.1002/2015PA002834

875 Kunzmann, M., Halverson, G. P., Sossi, P. A., Raub, T. D., Payne,
876 J. L., Kirby, J., 2013. Zn isotope evidence for immediate resumption
877 of primary productivity after snowball Earth. Geology 41 (1), 27–30.
878 http://dx.doi.org/10.1130/G33422.1

879 Lazar, B., Erez, J., 1992. Carbon geochemistry of marine-derived brines: I.
880 ^{13}C depletions due to intense photosynthesis. Geochimica et Cosmochimica
881 Acta 56 (1), 335–345. http://dx.doi.org/10.1016/0016-7037(92)90137-8

882 Liu, C., Wang, Z., Macdonald, F. A., 2018. Sr and Mg isotope geochemistry
883 of the basal Ediacaran cap limestone sequence of Mongolia: Implications
884 for carbonate diagenesis, mixing of glacial meltwater, and seawater chem-
885 istry in the aftermath of Snowball Earth. Chemical Geology 491, 1–13.
886 https://doi.org/10.1016/j.chemgeo.2018.05.008

887 Liu, C., Wang, Z., Raub, T. D., Macdonald, F. A., Evans, D. A.
888 D., 2014. Neoproterozoic cap-dolostone deposition in stratified glacial
889 meltwater plume. Earth and Planetary Science Letters 404, 22–32.
890 http://dx.doi.org/10.1016/j.csr.2013.08.007

891 Macdonald, F. A., McClelland, W. C., Schrag, D. P., Macdonald, W. P.,
892 2009. Neoproterozoic glaciation on a carbonate platform margin in Arctic

Alaska and the origin of the North Slope subterrane. GSA bulletin 121 (3/4), 448–473. https://dx.doi.org/10.1130/B26401.1

Macdonald, F. A., Prave, A. R., Petterson, R., Smith, E. F., Pruss, S. B., Oates, K., Waechter, F., Trotzuk, D., Fallick, A. E., 2013a. The Laurentian record of Neoproterozoic glaciation, tectonism, and eukaryotic evolution in Death Valley, California. GSA Bulletin 125 (7-8), 1203–1223. http://dx.doi.org/10.1130/B30789.1

Macdonald, F. A., Strauss, J. V., Sperling, E. A., Halverson, G. P., Narbonne, G. M., Johnston, D. T., Kunzmann, M., Schrag, D. P., Higgins, J. A., 2013b. The stratigraphic relationship between the Shuram carbon isotope excursion, the oxygenation of Neoproterozoic oceans, and the first appearance of the Ediacara biota and bilaterian trace fossils in northwestern Canada. Chemical Geology 362, 250–272. https://dx.doi.org/10.1016/j.chemgeo.2013.05.032

Patterson, W. P., Walter, L. M., 1994. Depletion of ^{13}C in seawater CO_2 on modern carbonate platforms: Significance for the carbon isotopic record of carbonates. Geology 22 (10), 885–888. https://doi.org/10.1130/0091-7613(1994)022<0885:DOCISC>2.3.CO;2

Raub, T. D., 2008. Prolonged deglaciation of "Snowball earth" (Order No. 3317273). Available from ProQuest Dissertations and Theses Global; SciTech Premium Collection. (304390388). https://search.proquest.com/docview/304390388?accountid=13314

Reilly, T. E., Goodman, A. S., 1985. Quantitative analysis of saltwater-

freshwater relationships in groundwater systems – A historical perspective. Journal of Hydrology 80 (1), 125–160. https://doi.org/10.1016/0022-1694(85)90078-2

Rose, C. V., Maloof, A. C., 2010. Testing models for post-glacial 'cap dolostone' deposition: Nuccaleena Formation, South Australia. Earth and Planetary Science Letters 296 (3–4), 165–180. http://dx.doi.org/10.1016/j.epsl.2010.03.031

Shields, G. A., 2005. Neoproterozoic cap carbonates: a critical appraisal of existing models and the plumeworld hypothesis. Terra Nova 17 (4), 299–310. http://dx.doi.org/10.1111/j.1365-3121.2005.00638.x

Silva-Tamayo, J. C., Nägler, T. F., Sial, A. N., Nogueira, A., Kyser, K., Riccomini, C., James, N. P., Narbonne, G. M., Villa, I. M., 2010a. Global perturbation of the marine Ca isotopic composition in the aftermath of the Marinoan global glaciation. Precambrian Research 182 (4), 373–381. http://dx.doi.org/10.1016/j.precamres.2010.06.015

Silva-Tamayo, J. C., Nägler, T. F., Villa, I. M., Kyser, K., Vieira, L. C., Sial, A. N., Narbonne, G. M., James, N. P., 2010b. Global Ca isotope variations in c. 0.7 ga old post-glacial carbonate successions. Terra Nova 22 (3), 188–194. http://dx.doi.org/10.1111/j.1365-3121.2010.00933.x

Tang, J., Dietzel, M., Bhm, F., Khler, S., Eisenhauer, A., 2008. Sr^{2+}/Ca^{2+} and $^{44}Ca/^{40}Ca$ fractionation during inorganic calcite formation: II. Ca isotopes. Geochimica et Cosmochimica Acta 72 (15), 3733–3745. http://dx.doi.org/10.1016/j.gca.2008.05.033

939 Tipper, E. T., Galy, A., Gaillardet, J., Bickle, M. J., Elderfield, H., Carder, E.
940 A., 2006. The magnesium isotope budget of the modern ocean: Constraints
941 from riverine magnesium isotope ratios. Earth and Planetary Science Let-
942 ters 250 (1–2), 241–253. http://dx.doi.org/10.1016/j.epsl.2006.07.037

943 Trindade, R. I. F., Font, E., D'Agrella-Filho, M. S., Nogueira, A. C. R.,
944 Riccomini, C., 2003. Low-latitude and multiple geomagnetic reversals in
945 the Neoproterozoic Puga cap carbonate, Amazon craton. Terra Nova 15
946 (6), 441–446. https://doi.org/10.1046/j.1365-3121.2003.00510.x

947 Vahrenkamp, V. C., Swart, P. K., 1994. Late Cenozoic Dolomites
948 of the Bahamas: Metastable Analogues for the Genesis of Ancient
949 Platform Dolomites. Dolomites, Blackwell Publishing Ltd., 133–153.
950 http://dx.doi.org/10.1002/9781444304077.ch9

951 Wang, Z., Hu, P., Gaetani, G., Liu, C., Saenger, C., Cohen, A., Hart,
952 S., 2013. Experimental calibration of Mg isotope fractionation between
953 aragonite and seawater. Geochimica et Cosmochimica Acta 102, 113–123.
954 https://doi.org/10.1016/j.gca.2012.10.022

955 Wilson, A. M., 2005. Fresh and saline groundwater discharge to the
956 ocean: A regional perspective. Water Resources Research 41 (2).
957 http://dx.doi.org/10.1029/2004WR003399

958 Yang, J., Jansen, M. F., Macdonald, F. A., Abbot, D. S., 2017. Persistence of
959 a freshwater surface ocean after a snowball Earth. Geology 45 (7), 615–618.

960 Zeebe, R. E., Wolf-Gladrow, D., 2001. CO_2 in seawater: equilibrium, kinetics,
961 isotopes. Vol. 65. Elsevier Oceanography Series 65.

Appendix A. Geological Background

Appendix A.1. Congo Craton (Namibia)

The Keilberg cap dolostone (sections P4017, P7500, P7016, P7017) in northwest Namibia, the basal member of the Maieberg Fm., was deposited on the Congo paleocontinent overlaying the Ghaub glaciogenic unit or its correlative disconformity (Hoffman et al., 2007, 2011). The dolostone is thickest in sections on the outer platform (P7016 ∼100 m) and tapers to 15–20 m in sections on the inner platform (P4017, P7500) and 5 m in sections on the distal foreslope (P7017). The Keilberg cap dolostone has abundant wave-generated bedforms, such as low angle cross-bedding and giant wave ripples. Sections on the distal foreslope contain basal turbidites and sheet-crack cements. On the platform, the dolostone contains stromatolites with characteristic tubestone structures. The uppermost unit of the dolostone has thin-bedded marly dolomite, interpreted to be deposited during maximum flooding (Hoffman et al., 2007, 2011).

δ^{13}C values vary laterally across the Keilberg platform (Hoffman et al., 2007). Isotopic values from the lower slope section drop stratigraphically at the base of the dolostone from ∼0 to -3‰ over a few tens of centimeters. In contrast, δ^{13}C values from the outer platform are stable ∼-2‰ over >100 meters of stratigraphy, while values from the inner platform fall from ∼-3 to -5‰ over ∼20 meters of stratigraphy. Combined with this geochemical variability, detailed sedimentological evidence indicates that the Keilberg dolostone is diachronous with deposition from the deeper foreslope to the platform driven by sea level rise associated with ice-sheet melting (Hoffman et al., 2007).

The Maieberg Fm. above the Keilberg cap dolostone is composed of a thick deep-water limestone, with seafloor crystal fans, that transitions into an upper dolostone member, ending at a well-developed subaerial exposure surface (Hoffman, 2011). In this study, measurements from the middle Maieberg Fm. are restricted to one section deposited on the innermost platform (P4017). In this section, the middle Maieberg Fm. is composed entirely of limestone with consistently low δ^{13}C values $\sim$-6‰.

Appendix A.2. Kalahari Craton (Namibia)

The Dreigratberg cap dolostone in southwest Namibia (section F817) succeeds the Namaskluft glacigenic unit, deposited on the Kalahari paleocontinent (Macdonald et al., 2010; Hoffman and Macdonald, 2010). At the top of the escarpment above Namaskluft Farm, Cryogenian strata fills kilometers-wide paleocanyons, which are sealed by the Dreigratberg cap dolostone (Hoffman and Macdonald, 2010). The base of the Dreigratberg cap carbonate is characterized by a channelized $\sim$15 m thick package of turbiditic limestone. The limestone tapers out laterally and is succeeded by the dolostone, containing giant wave ripples and tubestone stromatolites. Sheet-crack cements occur near the base of the dolostone but are poorly developed and laterally discontinuous.

δ^{13}C values in the lower limestone unit of the Dreigratberg cap carbonate are slightly offset from the overlying dolostone unit (Macdonald et al., 2010; Hoffman and Macdonald, 2010). The limestone unit has δ^{13}C values $\sim$-4‰ whereas the overlying dolostone has values $\sim$-3‰.

Appendix A.3. South Australia

The Nuccaleena Fm. of the Adelaide Rift Complex (ARC), South Australia, exhibits many of the unique sedimentary features observed in other basal Ediacaran cap dolostone units. The Nuccaleena cap dolostone (sections N250, N255, N288, C212, C213, C215) is deposited across a central anticline representing a shelf setting and a series of south-facing half-graben structures to the north that span upper slope to basinal settings (Rose and Maloof, 2010). The thickest dolostone units are found in the northernmost part of the Adelaide Rift Complex, interpreted as the most distal depositional setting (C215, C212, C213, N288) and taper towards the shallower depositional settings in the south (N250, N255). The Nuccaleena cap dolostone consists of four main lithofacies (Rose and Maloof, 2010) that are comparable to the lithofacies listed from Namibia (see above): Low-angle cross-stratified dolomite grainstone, grainstone with "giant wave ripples", isopachous sheet-crack cements, and low-angle cross-stratified ribbon facies. The sheet-crack cements within the Nuccaleena cap dolostone are restricted to the more distal depositional settings in the north of the Adelaide Rift Complex, while the "giant wave ripples" are found across the ARC but best developed in the shallower settings towards the south.

Within individual sections of the Nuccaleena cap dolostone δ^{13}C values span a few per mil but record a wide range of more than 7‰ across the Adelaide Rift Complex. In sections south of the Mt Fitton anticline, both shallow and deeper sections have δ^{13}C values decreasing stratigraphically from ∼-2 to -4‰ (N250, N255, N288). North of the Mt Fitton anticline, the shallower sections have values between -4 and -8‰ (C212, C213), while

the most distal section (C215) have values that gradually increase from -2 to +2‰.

Appendix A.4. Laurentia (Death Valley)

The Noonday cap dolostone in Death Valley was deposited on the southwestern margin of Laurentia, succeeding the glaciogenic Kingston Peak Fm. The Noonday cap dolostone sections (F1344, F1340 F1341) measured in this study follow a north to south transect from the platformal "Nopah facies" to the basinal "Ibex facies" (Macdonald et al., 2013a). The thickest section is composed of platform dolostone from the Sentinel Peak Member in the northern Saddle Peak Hills (F1344 ∼125 m), consisting of microbial peloidal dolostone, tubestone stromatolites, and sheet-crack cements. The dolostone tapers towards the south and the basinal section in Bunny Hills (F1341 ∼40 m) consists of thinly-laminated micritic limestone interrupted by dolostone olitholiths that were transported from the platform (Macdonald et al., 2013a). The most distal section from the Silurian Hills (F1340 ∼10 m) consists entirely of thinly-laminated micritic limestone representative of a lower-slope environment.

In contrast to cap dolostone sections from South Australia and Namibia, the cap carbonate of the Noonday Sentinel Peak Member has a smaller range in δ^{13}C values both within individual sections and across the basin. The more distal limestone units of the Noonday cap carbonate have δ^{13}C values that increase stratigraphically from ∼-6 to -4‰. The platform dolostones have more constant values ∼-3‰.

Appendix A.5. Laurentia (Northwest Canada)

The Ravensthroat cap dolostone of the Mackenzie Mountains (or "Tepee" dolostone of Eisbacher, 1981) was deposited along the northwestern margin of Laurentia, where it succeeds the glaciogenic Stelfox Member of the Ice Brook Fm. (Macdonald et al., 2013b; Aitken, 1991; James et al., 2001). In the Mackenzie Mountains, the Ravensthroat Fm. is ∼0–18 m thick and is overlain by 0–10 m of limestone with pseudomorphic aragonite fans that comprises the informal Hayhook Fm. (James et al., 2001). The J1132 and P7D sections were measured near the Shale Lake locality and were deposited along the platform edge. Both sections contain characteristic cap dolostone sedimentary features such as micropeloidal dolostone, tubestone stromatolites, and giant wave ripples (Macdonald et al., 2013b). The δ^{13}C values in the dolostone unit are relatively stable ∼-3.5‰ but drop to values ∼-5‰ in the overlying Hayhook limestone (Macdonald et al., 2013b).

The Ravensthroat cap dolostone of the Hay Creek Group of the Ogilvie Mountains (J1713) consists of finely laminated dolostone with sheet-crack cements and giant wave ripples that was deposited on the glacigenic Eagle Creek Formation of the Rapitan Group (Strauss et al., 2014; Macdonald et al., 2013b). The cap dolostone is ∼10 m thick and succeeded by a thick unit of black shale. Section J1713 record δ^{13}C values that decrease stratigraphically from ∼-0.5 to -3.5‰.

The Ravensthroat cap carbonate from the Tatonduk region of Alaska and Yukon (J1402) is correlative with the cap carbonate succession of the Coal Creek inlier of the Ogilvie Mountains (Macdonald et al., 2011). These strata consist of ∼9–12 m of buff yellow finely laminated dolomudstone and

grainstone with sheet-crack cements and rare giant wave ripples that were most likely deposited on the inner to outer platform. At this locality, the $\delta^{13}C$ values are stratigraphically more variable and increase from ∼-7 to -2‰ over a few meters at the base of the section.

Appendix A.6. Laurentia (Arctic Alaska)

Although no glacial diamictites have been identified, the Nularvik cap carbonate contains many of the sedimentological features associated with basal Ediacaran cap carbonates, such as giant wave ripples, tubestone stromatolites, isopachous cements, and relict aragonite crystal fans (Macdonald et al., 2009). The Nularvik cap carbonate (K2 unit) from the Sadlerochit Mountains in Alaska (section F601) is part of a thick (∼530 m) sequence of carbonate strata of the Katakturuk Dolomite (K1 unit), deposited directly on top of a prominent exposure surface (Macdonald et al., 2009; Strauss et al., in press). The $\delta^{13}C$ values in section F601 vary between ∼0 and -2‰.

Appendix A.7. Mongolia

The cap dolostone of the Ol Fm. in Mongolia (sections F860, F708, F875, U1113) was deposited in the Zavkhan Terrane, succeeding the Marinoan glacigenic Khongor Fm. (Bold et al., 2016). These carbonates were deposited on a passively subsiding carbonate ramp and are generally composed of finely-laminated micropeloidal dolomite with tubestone stromatolites and giant wave ripples (Bold et al., 2016) – consistent with many of the features associated with basal Ediacaran cap dolostones worldwide. However, in some locations the dolostone is heavily recrystallized (Bold et al., 2016). Towards the top of the Ol Fm., the dolostone hosts aragonite and barite crystal fans

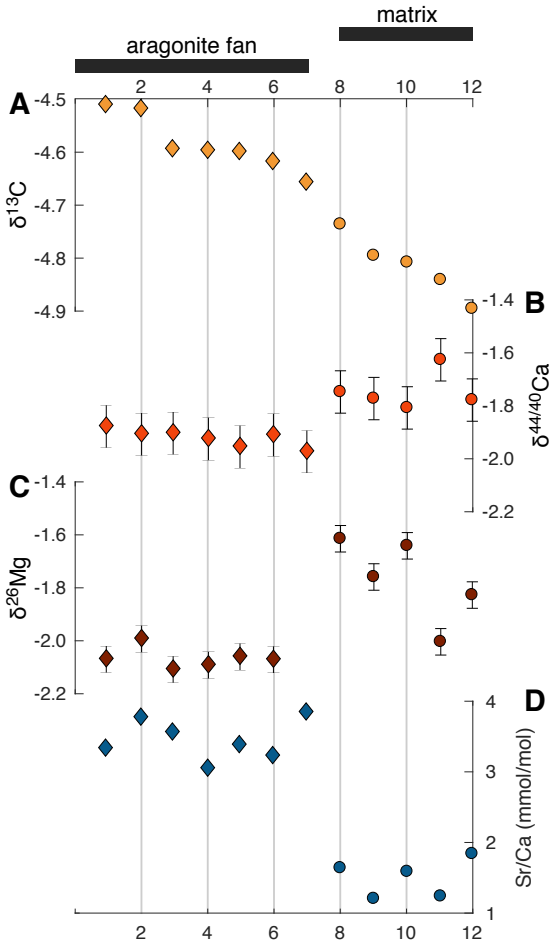

Figure A.10: **Selected sampling of aragonite fans (diamonds) and matrix (circles) from the Hayhook Fm., Northwest Canada** Numbers 1-7 represent grey pseudomorphic aragonite fans and numbers 8-12 represent red mud matrix. The mineralogy today is low-Mg calcite. (A) δ^{13}C values, (B) $\delta^{44/40}$Ca values, (C) δ^{26}Mg values, and (D) Sr/Ca ratios (mmol/mol).

and is succeeded by the Shuurgat Fm., containing the maximum postglacial flooding surface.

Sections F875 and U1113 were deposited in relatively more proximal settings compared to sections F708 and F860. In these shallower settings (F875, U1113), glacial-interlude sediments stratigraphically below the Ol cap dolostone are pervasively dolomitized, which appears to influence the geochemistry of the overlying dolostone (Bold et al., 2016). The δ^{13}C values range from -5 to +2‰ in U1113 and from +2 to +6‰ in F875 (Bold et al., 2016). In the more distal sections (F860, F708) the glacial-interlude sediments are primarily composed of limestone and the overlying dolostone units are composed of finely-laminated micropeloidal dolomite with giant wave ripples. δ^{13}C values in these dolostone units are generally lower compared to the shallower settings, ranging from -6 to 0‰.

Appendix A.8. Dolomitization in Mongolia

The geochemical signature of cap dolostone samples from Mongolia are consistently offset from sections in Australia, Namibia, and North America. Specifically, the δ^{13}C values of the Mongolian samples are higher than in other sections with values up to +8‰. The range in values observed in Mongolia previously has been linked to a regional expansive dolomitization front (Bold et al., 2016). The covariation between δ^{13}C, $\delta^{44/40}$Ca and δ^{26}Mg values are consistent with this interpretation and indicate that δ^{13}C values were reset towards higher values during dolomitization. This dolomitization front penetrates the basal Ediacaran dolostone and the underlying glacial and pre-glacial sediments where δ^{13}C values also have been reset (Bold et al., 2016). Moreover, by comparison to our results from other cap carbonate

sections it appears that the dolomitizing fluid in Mongolia was significantly modified from either glacial seawater or meltwater. As a result, we attribute the enriched δ^{13}C values in the Mongolia cap dolostone to the local history of dolomitization and fluid flow (Bold et al., 2016).

Appendix B. Methods

Appendix B.1. Sample dissolution

For each sample ∼5 mg of carbonate powder was dissolved in 5 mL 0.1 N buffered acetic acid (pH∼5). The solution was placed in a 15 mL Falcon centrifuge tube and allowed to react in an ultra-sonicator for 4 hrs. Each solution was centrifuged at 2500 rpm for 30 mins before pipetting off the upper 3 mL of supernatant into a new Falcon tube that had been pre-rinsed in MilliQ water. This procedure readily dissolves limestone and dolomite but leaves less soluble sediment components unreacted.

Appendix B.2. $\delta^{13}C$ and $\delta^{18}O$ measurements

δ^{13}C and δ^{18}O measurements were not performed in this study. Instead, δ^{13}C and δ^{18}O values are reported from previous published studies, where measurements were performed on the same sample sets (Bold et al., 2016; Macdonald et al., 2013b; Hoffman and Macdonald, 2010; Macdonald et al., 2009; Hoffman et al., 2007; Rose and Maloof, 2010).

Appendix B.3. $\delta^{44/40}Ca$ and $\delta^{26}Mg$ measurements

At Princeton University, samples were processed for Ca and Mg isotope analyses using an automated high-pressure ion chromatography system (IC,

Dionex UCS-5000+) to isolate either Ca or Mg in agreement with methods outlined in (Higgins et al., 2018; Blättler et al., 2015; Husson et al., 2015). The purified samples were analyzed for $\delta^{44/40}$Ca and δ^{26}Mg values on a Thermo Scientific Neptune Plus MC-ICP-MS. The analyses were performed using standard sample-standard bracketing methods to correct for instrumental mass bias. Measurements were carried out at low resolution for Mg and medium resolution for Ca to avoid $ArHH^+$ interferences. All samples were diluted to match standard concentrations within 0–10% to ensure comparable levels of $ArHH^+$-based interference across samples and standards and to minimize concentration-dependent isotope effects. All samples were measured twice within the same run and a subset of samples were remeasured in subsequent runs. All data are reported in delta notation relative to a known standard: For Ca isotopes, the measured $\delta^{44/42}$Ca values are converted to $\delta^{44/40}$Ca values relative to modern seawater assuming mass dependent fractionation with a slope of 2.05. For Mg isotopes, measured δ^{26}Mg values are reported relative to Dead Sea Metal (DSM-3). Long-term external reproducibility for each isotopic system is determined based on the standard deviation of known standards taken through the full chemical procedure with each batch of samples. For Ca isotopes, the external reproducibility for SRM915b and SRM915a relative to modern seawater is -1.19 ± 0.14‰ (2σ, N=120) and -1.86 ± 0.16‰ (2σ, N=24), respectively. For Mg isotopes, the long-term external reproducibility for Cambridge-1 and seawater are -2.61 ± 0.10‰ (2σ, N=81) and -0.83 ± 0.10‰ (2σ, N=47), respectively.

Appendix B.4. Major and trace element analysis

The Sr/Ca (mmol/mol), Mn/Ca (mmol/mol), and Mg/Ca (mol/mol) ratios were measured on aliquots of dissolved powders analyzed for $\delta^{44/40}$Ca and δ^{26}Mg isotopes using a Thermo Finnegan iCAP Q Inductively Coupled Plasma Mass Spectrometer (ICP-MS). The metal to calcium ratios were determined using a set of matrix-matched in-house standards spanning the sample range. The external reproducibility of the ratios is estimated at <10% (N=29) from replicate measurements of SRM-88b.

Appendix C. Diagenetic model sensitivity tests

The diagenetic model is used to simulate two different scenarios: (1) early dolomitization in glacial seawater and (2) aragonite neomorphism in the meltwater surface ocean. To evaluate these two model scenarios, the dataset has been split into dolomites (aragonite dolomitized in glacial seawater) and limestones (aragonite neomorphosed in meltwater). In each model scenario, the composition of the primary sediment is set to match the more sediment-buffered samples in the dataset (indicated by the lowest $\delta^{44/40}$Ca values). For the glacial seawater model, the primary sediment is set to a δ^{13}C value of -5‰, a $\delta^{44/40}$Ca value of -2.1‰, and a δ^{26}Mg value of -1‰. For the meltwater surface ocean model, the primary sediment has a δ^{13}C value of -4.5‰, a $\delta^{44/40}$Ca value of -2.1‰, and a δ^{26}Mg value between -1 to -2‰. The range in δ^{26}Mg values of the primary sediment are interpreted to reflect aragonite precipitation from a heterogenous Mg pool in the surface meltwater ocean as a result of a small degree of mixing with more Mg-rich seawater across the continental margin.

The composition of the diagenetic fluids (glacial seawater and meltwater) are estimated by optimizing the model fit to the geochemical dataset for cap dolostones and limestones, respectively. When optimizing the model for each model scenario, samples that are judged to be affected by both seawater and meltwater diagenesis are ignored (F817, C212, J1402, J1132, F1340).

The model fit is evaluated through three parameters: the residual, model size, and accuracy: First, the residual measures the fit between the model phase-space and the distribution of data points (i.e., assessing if the model phase-space covers the entire data range). The residual is calculated as the orthogonal distance between each sample and the model phase-space and is normalized for the ranges of each individual proxy. For example, a residual value of 0 means that all data points are encompassed by the model phase-space across all four cross-plots ([1] $\delta^{44/40}$Ca versus δ^{13}C values, [2] $\delta^{44/40}$Ca versus Sr/Ca ratios, [3] $\delta^{44/40}$Ca versus δ^{26}Mg values, [4] δ^{13}C versus δ^{26}Mg values). In contrast, a residual value of 1 means that all data points are outside the model phase-space. Second, to limit the size of the model phase-space to the tightest possible fit to the data set, the model size is added to the residual by calculating the ratio between the range in data relative to the range of the model (1- model range/data range), averaged across the four proxies. Third, the accuracy measures the consistency of the model in predicting the degree of alteration across different pairs of proxies (i.e., the percentile of mixing between primary aragonite and secondary dolomite). For example, if the model predicts 80% alteration for a specific sample in the cross-plot of $\delta^{44/40}$Ca versus δ^{26}Mg values, the prediction should hold in the cross-plot of δ^{26}Mg versus δ^{13}C values. For the glacial seawater model

scenario, the model accuracy is calculated as the 1σ standard deviation of the predicted % alteration for each sample across the four cross-plots. Due to the smaller size of the limestone data set, for the meltwater model scenario the accuracy is calculated as 0.5σ standard deviation of the % alteration for each sample (i.e. the weight of the misfit for a single sample in the meltwater model is reduced to match the glacial seawater model scenario) .

Based on the three parameters outline above, model results for the diagenetic fluid are optimized by minimizing the model cost function: $residual + modelsize + accuracy$ (Fig. C.11–C.12). Model results indicate that glacial seawater had a Mg/Ca ratio of ∼0.9, a $\delta^{44/40}$Ca value of -0.6‰, a δ^{26}Mg values of -0.2‰, and a δ^{13}C value of +2‰ (Fig. C.11). Glacial seawater δ^{13}C values may be overestimated based on unusually enriched δ^{13}C values from a single section (C215, South Australia). When disregarding this particular section, model results indicate a δ^{13}C value of glacial seawater of ∼0‰. Based on the geochemical signature of the cap limestones, model results indicate that the meltwater surface ocean had Mg/Ca ratios of ∼0.025, a $\delta^{44/40}$Ca value of -0.4‰, a δ^{26}Mg values of -1.8‰, and a δ^{13}C value of ∼-11‰ (Fig. C.12).

It should be noted that the model estimates for the isotopic composition of the diagenetic fluids (seawater and meltwater) are subject to variations in the isotopic fractionation factor, where any change in the fluid value can be compensated by changing the isotopic fractionation factor (Table C.2). Similarly, model results for the elemental concentrations of the diagenetic fluids are scaled relative to each other (i.e. a doubling of the concentration of C, Ca, and Mg would yield the same model phase-space).

Supplemental Reference List

Aitken, J.D., 1991. The Ice Brook Formation and post-Rapitan, Late Proterozoic glaciation, Mackenzie Mountains, Northwest Territories. Geological Survey of Canada Bulletin 404, 43 p.

Eisbacher, G.H., 1981. Sedimentary tectonics and glacial record in the Windermere Supergroup, Mackenzie Mountains, northwestern Canada. Geological Survey of Canada Paper 80-27, 40 p.

James, N., Narbonne, G., and Kyser, T., 2001, Late Neoproterozoic cap carbonates: Mackenzie Mountains, northwestern Canada: precipitation and global glacial meltdown: Canadian Journal of Earth Sciences, 38 (8), 1229–1262.

Macdonald, F.A., Strauss, J.V., Rose, C. V., Dudás, F. Ő., Schrag, D. P., 2010. Stratigraphy of the Port Nolloth Group of Namibia and South Africa and implications for the age of Neoproterozoic iron formations. American Journal of Science, 310 (9), 862–888.

Macdonald, F.A., Smith, E.F., Strauss, J.V., Cox, G.M, Halverson, G.P. and Roots, C.F., 2011. Neoproterozoic and early Paleozoic correlations in the western Ogilvie Mountains, Yukon: in, Yukon Exploration and Geology 2010, K.E. MacFarlane, L.H. Weston and C. Relf (eds.), Yukon Geological Survey, p. 161-182.

Strauss, J.V., Roots, C.F., Macdonald, F.A., Halverson, G.P., Eyster, A., and Colpron, M., 2014. Geological map of the Coal Creek inlier, Ogilvie

Mountains (NTS 116B/10-15 and 116C/9, 16). Yukon Geological Survey, Open File 2014-15, 1:100,000, 1 sheet.

Strauss, J.V., Macdonald, F.A., and McClelland, W.C., in press. Pre-Mississippian stratigraphy and provenance of the North Slope subterrane of Arctic Alaska I: Platformal rocks of the northeastern Brooks Range and their significance in circum-Arctic evolution, in Piepjohn, K., Strauss, J.V., Reinhardt, L. and McClelland, W.C., eds., Circum-Arctic Structural Events: Tectonic Evolution of the Arctic Margins and Trans-Arctic Links with Adjacent Orogens: Geological Society of America Special Papers.

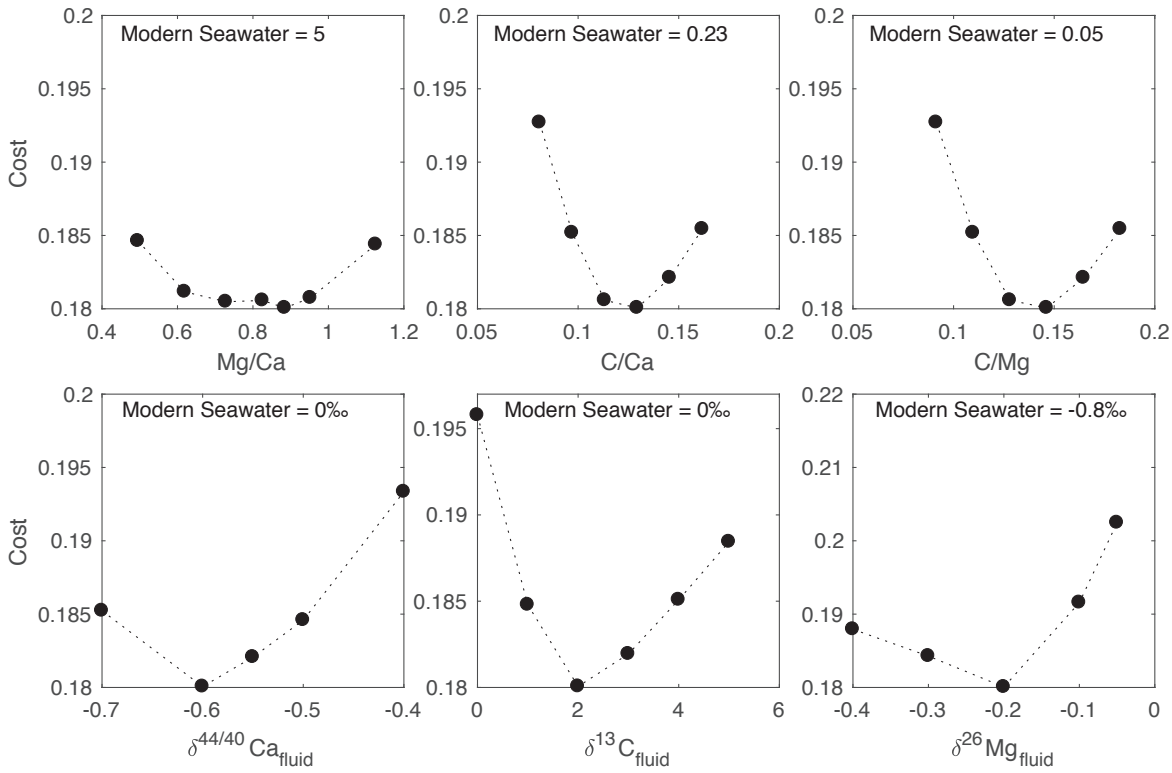

Figure C.11: **Model optimization for glacial seawater** The y-axis shows the total cost (the sum of the residual, accuracy, and model size) and the x-axis indicate the specific parameter in question **A** Mg/Ca ratio of seawater, **B** C/Ca ratio of seawater, **C** C/Mg ratio of seawater, **D** $\delta^{44/40}$Ca value of seawater, **E** δ^{13}C value of seawater, **F** δ^{26}Mg value of seawater. The red line illustrates the range in model estimates given a 1% change to the model cost. The composition of modern seawater is indicated on each subplot.

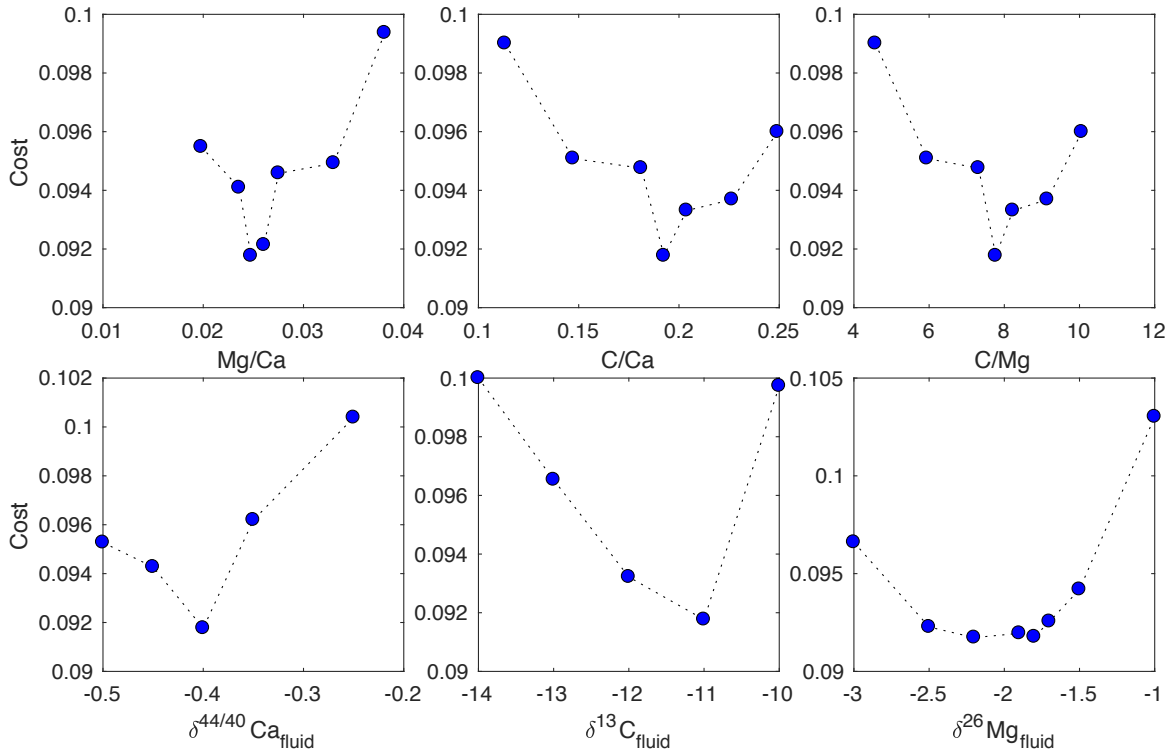

Figure C.12: **Model optimization for meltwater** The y-axis shows the total cost (the sum of the residual, accuracy, and model size) and the x-axis indicate the specific parameter in question **A** Mg/Ca ratio of meltwater, **B** C/Ca ratio of meltwater, **C** C/Mg ratio of meltwater, **D** $\delta^{44/40}$Ca value of meltwater, **E** δ^{13}C values of meltwater, **F** δ^{26}Mg values of meltwater. The red line illustrates the range in model estimates given a 1% change to the model cost.

Table C.2: Summary of model notation and parameters (see Ahm et al. (2018) for details on model setup)

Parameter	Definition	Meltwater model	Seawater model
α_{Ca}	Ca isotopic fractionation factor for diagenesis	1.000	1.000
α_{Mg}	Mg isotopic fractionation factor	0.9975	0.9980
α_C	C isotopic fractionation factor	1.001	1.0025
K_{Sr}	Distribution coefficient for Sr	0.01	0.01
R	Reaction rate constant	1% kyr^{-1}	1% kyr^{-1}
u	Advection rate	1.2 m/yr	1.2 m/yr
m	Stoichiometric scaling factor for Mg/C	0.001	0.5
M_f	Mass of element in fluid (mmol/kg)	C = 4.8 Ca = 18.1 Sr = 0.09 Mg = 0.5	C = 1.9 Ca = 14.9 Sr = 0.09 Mg = 13.2
M_s	Mass of element in primary sediment	C = 12% Ca = 39% Sr = 5000 ppm Mg = 5000 ppm	C = 12% Ca = 39% Sr = 5000 ppm Mg = 5000 ppm
δ_f	Isotopic value of fluid	δ^{13}C = -11‰ δ^{44}Ca = -0.4‰ δ^{26}Mg = -1.8‰	δ^{13}C = 2‰ δ^{44}Ca = -0.6‰ δ^{26}Mg = -0.2‰
δ_s	Isotopic value of primary sediment	δ^{13}C = -4.5‰ δ^{44}Ca = -2.1‰ δ^{26}Mg = -1‰	δ^{13}C = -5.0‰ δ^{44}Ca = -2.1‰ δ^{26}Mg = -1‰
Φ	Porosity	0.5	0.5
V	Box volume	1 m^3	1 m^3
ρ_s	Density of solid	1.8 g/cm^3	1.8 g/cm^3
ρ_f	Density of fluid	1.0125 g/cm^3	1.0125 g/cm^3
n	box number	75	19